



1 **Understanding influence of ocean waves on Arctic sea ice simulation: A modeling study**
2 **with an atmosphere-ocean-wave-sea ice coupled model**

3

4 **Chao-Yuan Yang¹, Jiping Liu², Dake Chen¹**

5

6 ¹Southern Marine Science and Engineering Guangdong Laboratory (Zhuhai), Zhuhai,
7 Guangdong, China

8 ²Department of Atmospheric and Environmental Sciences, University at Albany, State
9 University of New York, Albany, NY, USA

10

11 Corresponding authors:

12 Chao-Yuan Yang (yangchaoyuan@sml-zhuhai.cn) and Jiping Liu (jliu26@albany.edu)

13

14



15 **Abstract**

16 Rapid decline of Arctic sea ice has created more open water for ocean wave development
17 and highlighted the importance of wave-ice interactions in the Arctic. Some studies have made
18 contributions to our understanding of the potential role of the prognostic floe size distribution
19 (FSD) on sea ice changes. However, these efforts do not represent the full interactions across
20 atmosphere, ocean, wave, and sea-ice. In this study, we implement a modified joint floe size
21 and thickness distribution (FSTD) in a newly-developed regional atmosphere-ocean-wave-sea
22 ice coupled model and conduct a series of pan-Arctic simulation with different physical
23 configurations related to FSD changes, including FSD-fixed, FSD-varied, lateral melting rate,
24 wave-fracturing formulation, and wave attenuation rate. Firstly, our atmosphere-ocean-wave-
25 sea ice coupled simulations show that the prognostic FSD leads to reduced ice area due to
26 enhanced ice-ocean heat fluxes, but the feedbacks from the atmosphere and the ocean partially
27 offset the reduced ice area induced by the prognostic FSD. Secondly, lateral melting rate
28 formulations do not change the simulated FSD significantly but they influence the flux
29 exchanges across atmosphere, ocean, and sea-ice and thus sea ice responses. Thirdly, the
30 changes of FSD are sensitive to the simulated wave height, wavelength, and wave period
31 associated with different wave-fracturing formulations and wave attenuation rates, and the
32 limited oceanic energy imposes a strong constraint for the response of sea ice to FSD changes.
33 Finally, our results also demonstrate that wave-related physical processes can have impacts on
34 sea ice changes with the constant FSD, suggesting the indirect influences of ocean waves on
35 sea-ice through the atmosphere and the ocean.



36 **1. Introduction**

37 Arctic sea ice, a major component in the climate system, has undergone dramatic changes
38 over the past few decades associated with global climate change. September and March Arctic
39 sea ice extent shows decreasing trends of -13.1% and -2.6% per decade from 1979 to 2020,
40 respectively (Perovich et al., 2020). The mean Arctic sea ice thickness has decreased by ~1.5-
41 2 meters from the submarine period (1958-1976) to the satellite period (2011-2018), largely
42 resulting from the loss of multiyear ice (Kwok, 2018; Tschudi et al., 2016). The drifting speed
43 of Arctic sea ice exhibits an increasing trend based on satellite and buoy observations (e.g.,
44 Rampal et al., 2009; Spreen et al., 2011; Zhang et al., 2022). As the Arctic Ocean has been
45 dominating by thinner and younger ice, Arctic sea ice is more likely to be influenced by
46 forcings from the atmosphere and the ocean.

47 Associated with the above Arctic sea ice changes, the Arctic fetch (open water area for
48 ocean wave development) is less limited by the ice cover. The increased Arctic fetch and
49 surface wind speed are able to lead to higher ocean waves in the Arctic Ocean based on
50 observations, reanalysis, and future projections (Casas-Prat and Wang, 2020; Dobrynin et al.,
51 2012; Liu et al., 2016; Stopa et al., 2016; Waseda et al., 2018). The higher ocean waves are
52 more likely to propagate deeper into the ice pack and have sufficient energy to break sea ice
53 into smaller floes (e.g., Kohout et al., 2014). Sea ice with mostly smaller floes has larger surface
54 area, particularly lateral surface. The increased lateral surface accelerates ice melting through
55 enhanced ice-ocean heat fluxes (e.g., Steele, 1992). Some studies also showed that the ice-floe
56 melting rate is a result of the interaction between floe size and ocean circulation (Gupta and



57 Thompson, 2022; Horvat et al., 2016). The enhanced ice melting creates more open water (i.e.,
58 fetch), which is a favorable condition for further wave development as well as the ice-albedo
59 feedback (Curry et al., 1995). These processes create a potential feedback loop between ocean
60 waves and sea ice (e.g., Asplin et al., 2014; Thomson and Rogers, 2014).

61 Arctic cyclones and their high surface wind are the important driver for large wave events
62 in the Arctic Ocean. Previous studies showed that intense storms like “Great Arctic Cyclone”
63 of 2012 (Simmonds and Rudeva, 2012) and strong summer cyclone in 2016 contribute to the
64 anomalously low sea ice extent in 2012 and 2016 (e.g., Lukovich et al., 2021; Parkinson and
65 Comiso, 2013; Peng et al., 2021; Stern et al., 2020; Zhang et al., 2013). Statistical analyses
66 based on cyclone-tracking algorithm across multiple reanalyses suggested that the number of
67 Arctic cyclones show a significantly positive trend in the cold season (e.g., Sepp and Jaagus,
68 2011; Valkonen et al., 2021; Zahn et al., 2018). The increased cyclone activities and more open
69 water areas cause more extreme wave events in the Arctic (e.g., Waseda et al., 2021).
70 Blanchard-Wrigglesworth et al. (2021) found that extreme changes in Arctic sea ice extent are
71 correlated with distinct wave conditions during the cold season based on the observations.

72 The potential feedback loop associated with ocean waves and sea ice and more extreme
73 wave events indicate the importance to represent these processes in climate models for
74 improving sea ice simulation and prediction (e.g., Collins et al., 2015; Kohout et al., 2014).
75 However, state-of-the-art climate models participating in the latest Coupled Model
76 Intercomparison Project Phase 6 (CMIP6) have not incorporated the interactions between
77 ocean waves and sea ice in their model physics (e.g., Horvat, 2021). The coupled effects of



78 ocean waves and sea ice include; the amplitude of ocean waves decays as the waves travel
79 under the ice cover due to the combination of scattering and dissipation (e.g., Squire, 2020).
80 Crests and troughs of ocean waves exert strains to sea ice, and sea ice breaks if the maximum
81 strain exceeds certain threshold (e.g., Dumont et al., 2011). The wave-induced ice breaking
82 changes the size of floes, which in turn changes the floe size distribution (FSD; Rothrock and
83 Thorndike, 1984). In addition to the interactions between ocean waves and sea ice, the floe size
84 contributes to the changes of atmospheric boundary layer (e.g., Schafer et al., 2015; Wenta and
85 Herman, 2019), mechanical responses of sea ice (e.g., Vella and Wettauer, 2008; Weiss and
86 Dansereau, 2017; Wilchinsky et al., 2010), the flux exchanges across air-sea ice-ocean
87 interfaces (Cole et al., 2017; Loose et al., 2014; Lu et al., 2011; Martin et al., 2016; Steele et
88 al., 1989; Tsamados et al., 2014), and the scattering of ocean wave propagation (e.g., Montiel
89 et al., 2016; Squire and Montiel, 2016). Thus, it is essential to have a prognostic FSD to
90 properly reflect wave-ice interactions as well as other processes related to the floe size in
91 climate models.

92 Recently, several studies have made contributions on understating responses of sea ice to
93 the prognostic FSD (e.g., Bateson et al., 2020; Bennetts et al., 2017; Boutin et al., 2020; Horvat
94 and Tziperman, 2015; Roach et al., 2018a, 2019; Zhang et al., 2015, 2016). However, these
95 studies used simplified model complexity (i.e., standalone sea ice model, ice-wave coupling,
96 ice-ocean coupling) and unable to give a full representation of sea ice responses under the
97 interactions across atmosphere, ocean, wave, and sea ice. Motivated by this, here we introduce
98 a newly-developed atmosphere-ocean-wave-sea ice coupled model, in which we implement



99 physical processes that simulate the evolution of floe size distribution. We use this new coupled
100 model to investigate the responses of sea ice to ocean waves, as well as interactions in the
101 Arctic climate system. This paper is structured as follows. Section 2 provides an overview of
102 the new coupled model, focusing on the wave component and the implementation of the
103 prognostic FSD. Section 3 describes the design of numerical experiments and the related model
104 configurations. Section 4 examines the responses of sea ice to wave-ice interactions with the
105 prognostic FSD, as well as other ocean waves-related processes. Discussions and concluding
106 remarks are provided in section 5.

107

108 **2. Model description**

109 The newly-developed atmosphere-ocean-wave-sea ice coupled model is based on
110 Coupled Arctic Prediction System (CAPS, Yang et al., 2022), which consists of the Weather
111 Research and Forecasting Model (WRF), the Regional Ocean Modeling System (ROMS), and
112 the Community Ice Code (CICE). The detailed description of each model component in CAPS
113 is referred to Yang et al. (2020; 2022). In this section, we focus on newly-added features in
114 CAPS as described below.

115 **2.1. Wave model component**

116 To represent wave-ice interactions, an ocean wave model is coupled into CAPS, which is
117 the Simulating Waves Nearshore (SWAN). SWAN is a third-generation wave model and
118 includes processes of diffraction, refraction, wave-wave interactions, and wave dissipation due
119 to wave breaking, whitecapping, and bottom friction (Booij et al., 1999). Recently, the SWAN



120 model has implemented wave dissipation due to sea ice based on an empirical formula, which
121 is called IC4M2 (Collins and Rogers, 2017; Rogers, 2019). Specifically, the temporal
122 exponential decay rate of wave energy due to sea ice is defined as,

$$125 \quad S_{ice}/E = -2c_g k_i \quad (1)$$

123 where S_{ice} is the sink term induced by sea ice, E is the wave energy spectrum, and c_g is the
124 group velocity. k_i is the linear exponential rate that is a function of frequency as follow,

$$129 \quad k_i(f) = c_0 + c_1 f + c_2 f^2 + c_3 f^3 + c_4 f^4 + c_5 f^5 + c_6 f^6 \quad (2)$$

126 where c_0 to c_6 are the user-defined coefficients and their values as described in Section 3. In
127 the SWAN model, both the wind source term S_{in} , and the sea ice sink term are scaled by sea
128 ice concentration a_{ice} , which is provided by the CICE model through the coupler in CAPS,

$$130 \quad S_{ice} \rightarrow a_{ice} S_{ice} \quad (3)$$

$$131 \quad S_{in} \rightarrow (1 - a_{ice}) S_{in} \quad (4)$$

132 2.2. Prognostic FSD

133 For the prognostic FSD implemented in the CICE model, we follow the joint floe size and
134 thickness distribution (FSTD; Horvat and Tziperman, 2015). The FSTD is defined as a
135 probability distribution $f(r, h) dr dh$. $f(r, h)$ represents the fraction of cell covered by ice with
136 floe size between r and $r + \Delta r$, thickness between h and $h + \Delta h$, and the FSTD satisfies,

$$139 \quad \int_{\mathcal{R}} \int_{\mathcal{H}} f(r, h) dr dh = 1 \quad (5)$$

137 The ice thickness distribution $g(h)$ (ITD; Thorndike et al., 1975), which is simulated by the
138 CICE model, and the FSD $F(r)$, can be obtained by integrating the FSTD over all floe sizes



140 and all ice thicknesses,

$$\int_{\mathcal{R}} f(r, h) dr = g(h) \quad (6)$$
$$\int_{\mathcal{H}} f(r, h) dh = F(r)$$

141 Roach et al. (2018a) suggested the modified FSTD, $L(r, h)$, to preserve the governing
142 equations of ITD in the CICE model, which satisfies,

$$\int_{\mathcal{R}} L(r, h) dr = 1 \quad (7)$$

144 and

$$f(r, h) = g(h) L(r, h) \quad (8)$$

145 As described in Roach et al. (2018a), the implementation of the modified FSTD ignores the
146 two-way relationship between floe size, that is, physical processes associated with FSD
147 changes (i.e., $L(r, h)$ changes) are independent across each ice thickness category. The
148 governing equation of FSTD is defined as,

$$\frac{\partial f(r, h)}{\partial t} = -\nabla \cdot (f(r, h) \vec{v}) + \mathcal{L}_T + \mathcal{L}_M + \mathcal{L}_W \quad (9)$$

151 The terms in the right-hand-side represent advection, thermodynamics, mechanical, and wave-
152 induced floe-fracturing processes. For these terms, except the last term \mathcal{L}_W , we follow the
153 approach described in Roach et al. (2018a) and related values for coefficients as described in
154 Section 3. The formulations of \mathcal{L}_W proposed in Horvat and Tziperman (2015) involves a
155 random function to generate sub-grid scale sea surface elevation to determine how floes are
156 fractured by ocean waves. As a consequence, simulations are not bitwise reproducible with the
157 formulation including a random function. To avoid this issue, we propose different approaches



159 for our implementation of FSTD as described below.

160 **2.3. Floe fracturing by ocean waves**

161 For the floe-fracturing term \mathcal{L}_W , we follow the formulation suggested by Zhang et al.
162 (2015), which has similar form as Horvat and Tziperman (2015) and can be described as,

$$168 \quad \mathcal{L}_W = -Q(r) f(r, h) + \int_{\mathcal{R}} \beta(r', r) Q(r') f(r', h) dr' \quad (10)$$

163 The first term in the right-hand-side represents the areal fraction reduction due to floe-
164 fracturing and the second term is the areal fraction gain from other floe size categories that
165 have floe-fracturing. In equation (10), $Q(r)$ is the probability that floe-fracturing occurs for
166 floe size between r and $r + \Delta r$, and $\beta(r', r)$ is the redistributor that transfers fractured floe
167 from floe size r' to r . \mathcal{L}_W does not create or destroy ice so it must satisfy,

$$170 \quad \int_{\mathcal{R}} \mathcal{L}_W dr = 0 \quad (11)$$

169 In this study, we propose two different formulations for $Q(r)$ and $\beta(r', r)$.

171 (a) Equally-redistribution

172 We follow the same assumption in Zhang et al. (2015). That is, ice-fracturing by ocean
173 waves is likely to be a random process and the size of fractured floe does not have favored floe
174 size based on aerial photographs and satellite images (e.g., Steer et al., 2008; Toyota et al.,
175 2006, 2011). Thus, fractured floe is equally-redistributed into smaller floe sizes. The
176 redistributor is defined as,

$$178 \quad \beta(r_1, r_2) = \begin{cases} 1/(c_2 r_1 - c_1 r_1) & \text{if } c_1 r_1 \leq r_2 \leq c_2 r_1 \\ 0 & \text{if } r_2 < c_1 r_1 \text{ or } r_2 > c_2 r_1 \end{cases} \quad (12)$$

177 where c_1 and c_2 are constants that define upper- and lower-bound of floe size redistribution.



179 Details of $\beta(r', r)$ in this formulation are referred to Zhang et al. (2015).

180 For the probability $Q(r)$, Zhang et al. (2015) used an user-defined coefficient to reflect
181 wave conditions and determine $Q(r)$. Zhang et al. (2016) suggested that the coefficient is a
182 function of wind speed, fetch, ITD, and FSD. Since CAPS has a wave component to simulate
183 wave conditions, we reformulate $Q(r)$ to include simulated wave information from the coupler
184 and $Q(r)$ is defined as,

$$191 \quad Q(r) = c_w H(\varepsilon) \exp \left[-\alpha \left(\frac{1-r}{r_{max}} \right) \right] \quad (13)$$

185 where $H(\varepsilon)$ is the Heaviside step function, the exponential function determines the fraction of
186 each floe size participating in fracturing, and user-defined coefficients, c_w and α , control the
187 upper-bound of $Q(r)$ and the shape of the exponential function. To include wave conditions
188 from the SWAN model, we apply the floe-fracturing parameterization suggested by Dumont et
189 al. (2011) to calculate the strain induced by ocean waves on ice floes, and use this
190 parameterization to define $H(\varepsilon)$ as,

$$198 \quad H(\varepsilon) = \begin{cases} 1, & \text{if } \varepsilon \geq \varepsilon_c \\ 0, & \text{if } \varepsilon < \varepsilon_c \end{cases} \quad (14)$$

$$199 \quad \varepsilon = \frac{2\pi^2 h_{ice} A_{wave}}{L_{wave}^2} \quad (15)$$

192 where the strain ε is proportional to the ice thickness h_{ice} and the mean amplitude of wave
193 A_{wave} , and inversely proportional to the square of the mean surface wavelength L_{wave} . If the
194 strain exceeds the strain yield limit ε_c (see Section 3), floe-fracturing occurs (i.e., $H(\varepsilon) = 1$).
195 The distribution of wave heights is, in general, a Rayleigh distribution, which allows us to use
196 the simulated significant wave height from the SWAN model to determine the mean wave
197 amplitude with following relationship (e.g., Bai and Bai, 2014),



201
$$A_{wave} = \frac{H_{wave}}{2} \cong \frac{5}{16} H_s \quad (16)$$

200 where H_{wave} is the mean wave height, and H_s is the significant wave height.

202 The exponential function is built on that the wave-strain on ice floes is separated by the
203 wavelength (e.g., Dumont et al., 2011, their Fig. 4). Floe size smaller than the wavelength is
204 more likely to move along with ocean waves with little bending (e.g., Meylan and Squire, 1994).
205 That is, the exponential function preferentially has higher fraction for larger floes.

206 (b) Redistribution based on a semi-empirical wave spectrum

207 As discussed in Dumont et al. (2011, their Fig. 4), fractured floes have a maximum size
208 with half of the surface wavelength. Thus, the wave distribution of different wavelengths in
209 each grid cells allows us to predict floe sizes after fracturing. The sea surface elevation is a
210 result of the superimposition of waves with different periods, amplitudes, and directions in
211 space and time. Empirical wave spectra have been proposed to describe wave conditions with
212 a finite set of parameters. Based on wave observations from a wide variety of locations,
213 Bretschneider (1959) suggested the formulation of wave spectrum, which are used to formulate
214 the redistribution of fractured-floe as described below.

215 The Bretschneider wave spectrum is defined as,

218
$$S_B(T) = \frac{1.25 H_s^2 T^5}{8 \pi T_p^4} \exp \left[-1.25 \left(\frac{T}{T_p} \right)^4 \right] \quad (17)$$

216 where T_p is the peak wave period, and the spectral wave amplitude is defined as (Dumont et
217 al., 2011),



$$A(T) = \sqrt{\frac{4\pi S_B(T)}{T}} \quad (18)$$

219 Similar to the distribution of wave height, Bretschneider (1959) found that the distribution of
220 wave period is, in general, a Rayleigh distribution and defined as,

$$P(T) = 2.7 \left(\frac{T}{T_{ave}}\right)^3 \exp\left[-0.675 \left(\frac{T}{T_{ave}}\right)^4\right] \quad (19)$$

222 where T_{ave} is the mean surface period. With the deep-water surface wave dispersion relation
223 $L(T) = gT^2/2\pi$, the corresponding wave length for each wave period bin can be obtained,
224 and the wave-strain distribution can be calculated with the modified equation (15),

$$\varepsilon(T) = \frac{2\pi^2 h_{ice} A(T)}{L(T)^2} \quad (20)$$

226 Combined with the Heaviside step function defined in the equation (14), the probability of floe-
227 fracturing for each wave period is obtained,

$$P_f(T) = H(\varepsilon(T)) \bar{P}(T) \quad (21)$$

229 where $\bar{P}(T)$ is the normalized $P(T)$. Based on $P_f(T)$ and the assumption that fractured floes
230 have a maximum size with half of the surface wavelength, the redistributor $\beta(r_1, r_2)$ can be
231 obtained based on following criteria: 1) floe size between r and $r + \Delta r$ (in radius) must be
232 greater than half of wavelength $L(T)$, 2) floes fractured by the wavelength $L(T)$ have the size
233 of $L(T)/2$, and 3) $P_f(T)$ represents the fraction of floe with r and $r + \Delta r$ transferred to new
234 size with r' and $r' + \Delta r$ determined by the criterion (2). The probability $Q(r)$ is the summation
235 of $P_f(T)$ and represents the total fraction of floe participating in wave-fracturing.

237 3. Model configurations and experiment designs

238 The model domain includes 320 (440) x- (y-) grid points with a ~24km resolution for all



239 model components (Fig. 1). Initial and boundary conditions for the WRF, ROMS, CICE models
240 are generated from the Climate Forecast System version 2 (CFSv2, Saha et al., 2014)
241 operational analysis, archived by National Centers for Environmental Information (NCEI),
242 National Oceanic and Atmospheric Administration (NOAA). In our configurations, the SWAN
243 model starts with the calm wave states (i.e., zero wave energy in all frequencies). The modified
244 FSTD, $L(r, h)$, is initialized based on the power-law distribution of floe number, $N(r) \propto r^{-a}$
245 (e.g., Toyota et al., 2006), with the exponent a as 2.1 for all grid cells. Physical
246 parameterizations of each model component are mostly identical to those used in Yang et al.
247 (2022) and summarized in Table 1.

248 Cassano et al. (2011) suggested that the use of a higher model top (10 mb) or applying
249 spectral nudging in the upper model levels lead to significantly reduced biases in pan-Arctic
250 atmospheric circulation in the standalone WRF model. Thus, compared with Yang et al. (2022),
251 we change the model top of the WRF model in CAPS from 50 mb to 10 mb. With coupling to
252 the SWAN model in CAPS, the corresponding configurations are modified to reflect wave
253 effects on the atmosphere and the ocean. In the Mellor-Yamada-Nakanishi-Niino planetary
254 boundary layer scheme (MYNN; Nakanishi and Nino, 2009), the surface roughness, z_0 , is
255 modified to include the effect of waves based on the following formulation,

259
$$z_0 = 1200H_s \left(\frac{H_s}{L_{wave}} \right)^{4.5} + \frac{0.11\nu}{u_*} \quad (22)$$

256 where ν is the viscosity, and u_* is the friction velocity (Taylor and Yelland, 2001; Warner et al.,
257 2010). For the interaction of ocean waves and currents, the vortex-force (VF) formulation is
258 applied that represents conservative (e.g., vortex and Stokes-Coriolis forces) and non-



260 conservative wave effects. The non-conservative wave effects in the VF formulation include
261 wave accelerations for currents and wave-enhanced vertical mixing (Kumar et al., 2012;
262 Uchiyama et al., 2010). The dissipated wave energy due to surface wave breaking and
263 whitecapping is transferred to the ocean surface layer as additional turbulent kinetic energy,
264 which in turn enhances the vertical mixing. For the effect of currents on the dispersion relation
265 in wave propagation, we employ a depth-weighted current to account for the vertically-sheared
266 flow following Kirby and Chen (1989). As discussed in previous studies (e.g., Naughten et al.,
267 2017; Yang et al., 2022), the upwind third-order advection (U3H, Table 1) scheme, which is an
268 oscillatory scheme, can lead to increased non-physical frazil ice formation. To address this
269 issue, we implement the upwind flux limiter suggested by Leonard and Mokhtari (1990) to
270 reduce false extrema caused by the oscillatory behavior of the U3H scheme. The value of
271 yielding strain ε_c , described in Section 2.3 is chosen as $\cong 3 \times 10^{-5}$ (Dumont et al., 2011;
272 Horvat and Tzipermann, 2015; Langhorne et al., 1998). The floe welding parameter in the
273 thermodynamic term \mathcal{L}_T , is chosen as $1 \times 10^{-7} \text{ km}^{-2} \text{ s}^{-1}$. Roach et al. (2018b) found a lower
274 bound of floe welding parameter as $1 \times 10^{-9} \text{ km}^{-2} \text{ s}^{-1}$ in the autumn Arctic based on the
275 observations. For the user-defined coefficients in the equation (4), all experiments use the
276 equally-redistributed formulation described in Section 2.3 with c_w as 0.8 and α as 1.0. Based
277 on the formation of \mathcal{L}_T in the equation (9) (see Roach et al., 2018a), the floe size change
278 through the lateral surface is determined by both the floe size and the lateral melting rate. In
279 the existing sea ice models, the lateral melting rate w_{lat} is all based on the empirical
280 formulation suggested by Perovich (1983, hereafter P83),



$$w_{lat} = m_1 \Delta T^{m_2} \quad (23)$$

281 where ΔT is the temperature difference between sea surface temperature (SST) and the freezing
282 point, and m_1 , m_2 are empirical coefficients based on the observations from a single sea ice
283 lead in the Canadian Arctic. This empirical formulation is also the default lateral melting rate
284 in the CICE model. Maykut and Perovich (1987, hereafter MP87) showed a different approach
285 to parameterize the lateral melting rate that includes the friction velocity u_* based on the
286 observations from the Marginal Ice Zone Experiment, which is defined as,

$$w_{lat} = u_* m_3 \Delta T^{m_4} \quad (24)$$

288 Both formulations (Equ. 23, 24) are examined in this study (see Table 2). In the equation (2),
289 the user-defined coefficients for the wave attenuation are set as $c_2 = 1.06 \times 10^{-3}$ and $c_4 =$
290 2.3×10^{-2} (case 1), which follow the polynomial of Meylan et al. (2014, hereafter M14) from
291 the observations with 10-25m floe in diameter in the Antarctic, and $c_2 = 2.84 \times 10^{-4}$ and
292 $c_4 = 1.53 \times 10^{-2}$ (case 2), which follow the polynomial of Rogers et al. (2018, hereafter R18)
293 based on the observations for pancake and frazil ice in the Arctic.

295 In this study, a series of numerical experiments for the pan-Arctic sea ice simulation have
296 been conducted, starting from January 1st 2016 to December 31st 2020. Table 2 provides the
297 details of the configurations for these experiments, which allow us to examine the influence of
298 ocean waves and related physical processes on Arctic sea ice simulation in the atmosphere-
299 ocean-wave-sea ice coupled framework. Specifically, these experiments focus on 1) the
300 comparison between constant FSD and prognostic FSD (Exp-CFSD and Exp-PFSD), 2) sea ice
301 responses to different lateral melting rate parameterizations (Exp-CFSD, Exp-PFSD, Exp-



302 LatMelt-C and Exp-LatMelt-P), 3) the difference between the equally-redistributed
303 formulation and the Bretschneider formulation for floe fracturing (Exp-PFSD and Exp-
304 WaveFrac-P), and 4) the contribution of different wave attenuation rates to sea ice changes
305 (Exp-CFSD, Exp-PFSD, Exp-WaveAtt-C and Exp-WaveAtt-P).

306 **4. Results**

307 **4.1 Constant vs. Prognostic floe size**

308 Figure 2 shows the evolution of sea ice area (SIA) for all experiments conducted in this
309 study (as well as the values of seasonal maximum and minimum SIA for all experiments are
310 summarized in Table S1). SIA is calculated as the sum of ice-covered area of all grid cells
311 (cell-area times sea ice concentration). In addition to the evolution of SIA, the 2016-2020
312 averaged March and September sea ice concentration (SIC) for all experiments are shown in
313 Figure S1. Compared with Exp-CFSD, which uses a constant floe diameter (300m) in the
314 lateral melting scheme (Steele, 1992), Exp-PFSD uses the equations described in Section 2.2
315 to determine the prognostic FSD and related physical processes (see Table 2). With the
316 prognostic FSD, the evolution of SIA in Exp-PFSD (Fig. 2a, red line) shows smaller SIA in the
317 melting months (June to September) and similar magnitude of SIA in other months compared
318 to that of Exp-CFSD (Fig. 2a, blue line) during 2016-2018. After that, Exp-PFSD simulates
319 smaller SIA than that of Exp-CFSD for most months during 2019-2020, especially for the
320 seasonal maximum of 2019 and SIA after May, 2020.

321 Figure 3 shows the evolution of sea ice mass budget terms with cell-area weighted
322 averaging over the entire model domain with 15-day running-average for smoothing out high-



323 frequency fluctuations for all experiments. The most notable difference between Exp-CFSD
324 and Exp-PFSD is the magnitude of basal melt (red lines) and lateral melt (grey lines). In Exp-
325 CFSD, basal melt plays the dominant role in reducing sea ice mass compared to lateral melt
326 that has negligible contribution to the total mass change. As discussed in Maykut and Perovich
327 (1987), the inclusion of friction velocity in calculating the lateral melting rate results in $w_{lat} \rightarrow$
328 0 as $u_* \rightarrow 0$, which contributes to negligible lateral melt in Exp-CFSD. By contrast, Exp-PFSD
329 with prognostic floe size shows that lateral melt has the major contribution in reducing ice mass
330 (Fig. 3b), a result of smaller floe size near the ice edge simulated by Exp-PFSD (Fig. 10a). It
331 is also notable that the increased lateral melt in Exp-PFSD tends to be compensated by the
332 decreased basal melt (Fig. 3b). The overall ice melt due to oceanic processes in Exp-PFSD (i.e.,
333 the sum of lateral melt and basal melt) does not change significantly compared to that of Exp-
334 CFSD (Fig. S2e). The melting potential in the CICE model of CAPS, the available energy from
335 the ocean to melt sea ice, is defined as the vertical integral of the difference between ocean
336 temperature and freezing point. When the available oceanic energy is less than the sum of heat
337 fluxes used for lateral and basal melt, the CICE model performs a linear scaling to maintain
338 the relative magnitude of heat fluxes for lateral and basal melt. Thus, the increased energy
339 consumption by lateral melt due to smaller floe size reduces the available energy for basal melt.
340 Such change between lateral and basal melt has been shown in some studies (e.g., Bateson et
341 al., 2020, 2022; Roach et al., 2018a, 2019; Smith et al., 2022; Tsamados et al., 2015). Although
342 the rough compensation, Exp-PFSD simulates more ice melted by the oceanic energy compared
343 to Exp-CFSD from January to July (Fig. S2e).



344 Figure 4 shows the evolution of ice-ocean heat flux, the friction velocity at the ice-ocean
345 interface, and the temperature difference between SST and freezing point for Exp-CFSD and
346 Exp-PFSD. These variables are the average of ice-covered cells with at least 1% ice
347 concentration, and the ice-ocean heat flux is weighted by the ice concentration so that the
348 weighted heat flux represents the mean value of cell, rather than the mean value of ice-ocean
349 interface. It should be noted that cells with negative values of the temperature difference (i.e.,
350 supercooled water) are forced to be zero. This is consistent with the treatment in the CICE
351 model for the calculation of ice-ocean heat flux. As shown in Fig. 4a and Fig. S2e, the evolution
352 of ocean-induced ice melt is consistent with that of the ice-ocean heat flux for both Exp-CFSD
353 and Exp-PFSD. Both Exp-CFSD and Exp-PFSD show relatively similar evolution of the
354 friction velocity (Fig. 4b). The temperature difference of Exp-PFSD is much smaller than that
355 of Exp-CFSD (Fig. 4c). The ice-ocean heat flux is the total heat flux from ocean to ice through
356 ice bottom surface and lateral surface. Although Exp-PFSD has smaller temperature difference
357 as well as the melting potential under ice-covered cells, the larger total ice surface area due to
358 smaller floe size increases the efficiency of Exp-PFSD extracting energy from the ocean. The
359 smaller temperature difference of Exp-PFSD and the compensation between lateral and basal
360 melt suggest that the ocean surface layer of Exp-PFSD is more closed to the freezing point
361 compared to that of Exp-CFSD. Energy loss from the ocean through air-sea heat flux that
362 further cools the upper ocean, freshwater input (e.g., ice melting, precipitation) that raises the
363 freezing point, as well as non-physical numerical oscillation (Naughten et al., 2018; Yang et
364 al., 2022) can lead to increased frazil ice formation of Exp-PFSD as shown in Fig. 3a-b and



365 Fig. S2g.

366 Figure 5 shows the heat flux budget at the ice surface averaged for all ice-covered cells.
367 The positive ice-atmosphere heat fluxes of Exp-CFSD and Exp-PFSD in July (Fig. S3a)
368 correspond to top melt in Fig. 3a-b and Fig. S2b (as well as Table S2). The ice-atmosphere heat
369 flux not only determines the magnitude of ice surface melt in summer but also the energy loss
370 from the ice interior in winter, which is crucial for the ice growth. As shown in Fig. S3a, Exp-
371 PFSD loses more energy to the atmosphere than that of Exp-CFSD in most winters. The
372 conductive heat flux also shows similar evolution, suggesting that more energy is conducted to
373 the ice top from ice layers below in Exp-PFSD (Fig. S3b). The loss of ice energy then
374 contributes to increased ice growth at the ice bottom as shown in Fig. 3a-b and Fig. S2f (as
375 well as Table S2). Generally, the net shortwave flux of Exp-PFSD is larger (ice gains more
376 energy) than that of Exp-CFSD, especially during the melting season (Fig. S3c). In contrast to
377 the net shortwave flux, for most of the time, the net longwave flux of Exp-PFSD is smaller (i.e.,
378 ice loses more energy) than that of Exp-CFSD (Fig. S3d). Exp-PFSD loses more energy
379 through sensible heat flux compared to Exp-CFSD (Fig. S3e). For latent heat flux, there is no
380 common features between Exp-PFSD and Exp-CFSD, suggesting the difference in the
381 simulation of atmospheric transient systems (Fig. S3f).

382 The ice mass budget in Fig. 3 is not directly related to the evolution of sea ice area in Fig.
383 2 since each process acts differently in changing ice area. For vertical processes (i.e., top melt,
384 basal melt), ice must be vertically-melted completely to reduce ice area. Lateral melt, on the
385 contrary, can directly reduce ice area (Smith et al., 2022). Figure 6 shows the evolution of sea



386 ice area changes due to thermal processes (top melt, basal melt, lateral melt, frazil ice formation)
387 and dynamical processes (transport, ridging). For thermal area changes, Exp-PFSD (red line),
388 in general, shows comparable ice area changes to increased ice area compared to Exp-CFSD
389 (blue line) for most of the period (Fig. 6a). Compared with Fig. S2g, the timings that Exp-
390 PFSD shows more thermally-increased ice area correspond to increased frazil ice formation,
391 which primarily occurs in open water. In contrast to thermal area changes, dynamical area
392 changes of Exp-PFSD tends to reduce ice area relative to that of Exp-CFSD (Fig. 6e).
393 Dynamically-induced area changes are partly due to the ridging scheme (Lipscomb et al., 2007)
394 that favors the conversion of thin ice to thicker ice and reduces total ice area but preserves the
395 total volume. In general, Exp-PFSD has higher fraction of ice in the thinner ITD range than
396 Exp-CFSD.

397 Based on geographic features, we define the following subregions for further analysis: 1)
398 Barents and Greenland Seas (ATL, 45W-60E, 65N-85N), 2) Laptev and Kara Seas (LK, 60E-
399 150E, 65N-85N), and 3) Beaufort, Chukchi, and East Siberian Seas (BCE, 150E-120W, 65N-
400 85N, see black boxes in Fig. 1 for the geographic coverage of subregions). The fetch of ATL,
401 LK and BCE regions are limited by the surrounding continents and the seasonal evolution of
402 ice-covered area. The ATL region is only partially-limited by ice-covered area while the LK
403 and BCE regions can be fully-covered by sea ice in winters. Figure 7 shows the evolution of
404 sea ice extent, sea ice area, domain-averaged significant wave height, melting potential, and
405 heat flux at the ocean surface ($FLUX_{OCN}$, including ice-ocean and atmosphere-ocean interfaces)
406 of Exp-CFSD and Exp-PFSD. As shown in Fig. 7a-c, it is clear that the higher (lower)



407 significant wave height corresponds to less (more) regional ice coverage for all subregions. For
408 the melting potential (Fig. 7d), the difference between Exp-CFSD (blue line) and Exp-PFSD
409 (red line) in August, in general, is correlated with $FLUX_{OCN}$ in July (Fig. 7e). The more (less)
410 incoming heat flux to the ocean due to less (more) ice-covered area increases (decreases)
411 energy stored in the ocean surface layer. However, $FLUX_{OCN}$ alone cannot explain the
412 difference of the melting potential for the entire period. For example, Exp-PFSD shows more
413 melting potential after December, 2019 in ATL region (Fig. d₁), and more melting potential in
414 December, 2017 in LK region (Fig. d₂) compared to Exp-CFSD. These timings do not show
415 corresponded $FLUX_{OCN}$ at the preceding month, suggesting the contribution of different
416 processes. Figure 8 shows the evolution of wave energy dissipation due to whitecapping and
417 the difference of temperature profile in the upper 150m for Exp-CFSD and Exp-PFSD. As
418 described in section 3, wave energy dissipation increases the turbulent kinetic energy in the
419 surface layer and thus vertical mixing. Dissipation due to surface wave breaking is zero for
420 most of the period. Occasionally, there are non-zero dissipations due to surface wave breaking
421 for Exp-CFSD and Exp-PFSD. The evolution of wave dissipation due to whitecapping (Fig.
422 8a-c) is in good agreement with that of significant wave height in Fig. 7c. This suggests that
423 stronger wave conditions associated with less ice-covered area increase the effect of vertical
424 mixing. Combined with the warmer upper ocean in Exp-PFSD after January, 2020 in ATL
425 region and in December, 2017 in LK region in Fig. 8d-e, the strengthened vertical mixing
426 brings warmer water of the subsurface upward and maintains/increases the melting potential in
427 the subregions.



428 Additionally, atmospheric circulation responds to the changes in spatial distribution of sea
429 ice (Fig. S1). As shown in Figure S4, Exp-PFSD tends to have anomalous anti-cyclonic
430 circulations in September compared to Exp-CFSD, but there is no consistent center of actions
431 during the entire period. In March, Exp-PFSD tends to simulate anomalous cyclonic
432 circulations in the Barents-Kara Sea for most of the years compared to Exp-CFSD, except 2019.
433 The response in the atmospheric state in both experiments also influence sea ice movement,
434 which further contributes to the regional ice differences in Fig. 7a-b, as well as the heat flux
435 budgets in Fig. S3.

436 **4.2 Sensitivity to lateral melting rate parameterization**

437 In addition to the floe size as discussed in the above section, the lateral melting rate (w_{lat})
438 is an important factor contributing the relative strength of lateral and basal melt. As described
439 in section 3, we conduct the experiments with the lateral melting rate suggested by Perovich
440 (1983, P83), and Maykut and Perovich (1987, MP87) (see Table 2), to examine the sensitivity
441 of Arctic sea ice simulation to different lateral melting rate parameterizations. As shown in Fig.
442 2b, the simulated summer sea ice area of Exp-LatMelt-C (green line) and Exp-LatMelt-P (grey
443 line), in general, is larger than those of Exp-CFSD (blue line) and Exp-PFSD (red line).

444 As shown in sea ice mass budget (Fig. 3a, 3c), Exp-LatMelt-C, which does not include
445 the friction velocity in the formulation (Equ. 23), but keeps other model configurations same
446 as Exp-CFSD only show slightly larger contribution to lateral melt during summer months (Fig.
447 S5d). Also, the contribution to basal melt by Exp-LatMelt-C is generally smaller than that in
448 Exp-CFSD (Fig. S5c). Similar to the experiments with MP87 scheme, Exp-LatMelt-P with the



449 prognostic FSD also shows the compensation between lateral melt and basal melt compared to
450 Exp-LatMelt-C (Fig. 3c, 3d). Exp-LatMelt-P show stronger lateral melt compared to Exp-
451 PFSD, which is contributed by the P83 formulation (Fig. S5d). Despite the stronger lateral melt
452 in Exp-LatMelt-P, its basal melt is smaller compared to Exp-PFSD (Fig. S5c). Thus, the ocean-
453 induced melt of Exp-LatMelt-P is broadly similar to that of Exp-PFSD. The result of Exp-
454 LatMelt-P and Exp-PFSD suggests that the changes of lateral and basal melt due to different
455 lateral melting rate parameterizations are mostly controlled by the available energy from the
456 ocean (i.e., melting potential).

457 Exp-LatMelt-P simulates more basal growth in winter (Fig. S5f), which is contributed by
458 more energy loss to the atmosphere (Fig. 5a), in comparison to Exp-PFSD. Also, more frazil
459 ice formation is simulated in Exp-LatMelt-P than Exp-PFSD during most of simulation period
460 (Fig. S5g). The combined effects of above processes lead to that Exp-LatMelt-P shows less
461 total ice melt in summer and similar ice growth in winter compared to Exp-PFSD (Fig. S5a).
462 Due to more frazil ice formation, Exp-LatMelt-P shows more thermally-increased ice area
463 compared to Exp-PFSD (Fig. 6, Fig. S5g). Frazil ice formation reduces open-water areas and
464 blocks the energy exchange between the atmosphere and the ocean. That is, the upper ocean
465 under sea ice in Exp-LatMelt-P receives less incoming flux from the atmosphere (i.e., solar
466 radiation) during April to September (not shown) to balance the energy consumption by ice
467 melt, which leads to smaller ocean temperature difference compared to Exp-PFSD (Fig. 4c,
468 green and red lines).

469 Figure 9 shows the spatial distribution of sea ice concentration, sea surface temperature,



470 and friction velocity in September, 2020 for the experiments using MP87 and P83 schemes.
471 Exp-CFSD, Exp-PFSD, and Exp-LatMelt-C simulate large areas with ice concentration less
472 than 5% (they are mostly much less than 1%, Fig. 9a₁₋₃). In opposite to these three experiments,
473 Exp-LatMelt-P does not show wide areas with non-zero and infinitesimal ice concentration
474 (Fig. 9a₄). Although these areas only account for a tiny fraction of total sea ice, they may still
475 be a source of uncertainty for sea ice simulations. Ice-existed cells can be influenced by all
476 processes involved in sea ice mass budget (Fig. 3) while ice-free cells can only be affected by
477 frazil ice formation and dynamical advection. Under these small-ice areas, SST is well above
478 the freezing point (Fig. 9b) and the friction velocity is mostly less than $5 \times 10^{-4} \text{ m/s}$ (Fig.
479 9c). In our configuration of CICE model, the minimum value of friction velocity is set to
480 $5 \times 10^{-4} \text{ m/s}$. This suggests that the friction velocity is the limit factor for heat flux
481 transferred into sea ice in the small-ice areas. For basal heat flux, the formulation in the CICE
482 model is based on Maykut and McPhee (1995), which is controlled by the friction velocity and
483 the temperature difference. Thus, basal heat fluxes with small friction velocities may not be
484 large enough to satisfy the energy convergence (in conjunction with conductive heat flux at the
485 ice bottom) at the ice-ocean interface to melt ice if the temperature difference does not show
486 larger magnitude. Since MP87 lateral melting scheme includes the friction velocity, lateral heat
487 flux is also limited in small-ice areas. Exp-PFSD has much smaller floe size (compared to
488 300m) in these small-ice areas, but the increased strength of lateral melt does not overcome the
489 limitation of friction velocity to melt ice completely (Fig. 9a₂). The P83 lateral melting scheme
490 that does not include the friction velocity is controlled by the temperature difference, but the



491 effect of lateral melting in Exp-LatMelt-C is largely constrained by constant 300m floe
492 diameter. Liang et al. (2019) suggested these small-ice areas can be eliminated by assimilating
493 SST observations. The results of Exp-LatMelt-P suggest a model physic approach that
494 considers the prognostic FSD and the lateral melting rate to reduce the coverage of small-ice
495 near the ice-edge.

496 **4.3 Sensitivity to floe-fracturing parameterization**

497 The equally-redistributed formulation (hereafter PF1) for floe-fracturing described in
498 section 2.3.a does not have preferential floe size after fracturing (i.e., a stochastic process).
499 However, the size of fractured floes can be predicted based on the properties of surface ocean
500 waves, particularly wavelength (Dumont et al. 2011; Horvat and Tziperman, 2015). In this
501 section, we conduct an experiment (Exp-WaveFrac-P, see Table 2), which utilizes a semi-
502 empirical wave spectrum to redistribute fractured floes (see section 2.3.b for details and
503 hereafter PF2) to explore the effects of different wave-fracturing formulations on Arctic sea ice
504 simulation. As shown in Fig. 2c, Exp-WaveFrac-P (orange line) simulates larger ice area in
505 summer and comparable ice area in winter with respect to Exp-PFSD (red line).

506 By applying different formulations for floe-fracturing (as well as different lateral melting
507 rate formulations), the FSD responds accordingly. To quantify the responses of FSD associated
508 with different physical configurations (Table 2), the representative floe radius r_a , as well as its
509 tendency due to different processes in the equation (9) are utilized and calculated as (Roach et
510 al., 2018a),



$$r_a = \frac{\int_{\mathcal{R}} \int_{\mathcal{H}} r f(r, h) dr dh}{\int_{\mathcal{R}} \int_{\mathcal{H}} f(r, h) dr dh} \quad (25)$$

$$\frac{dr_a}{dt} = \frac{\int_{\mathcal{R}} \int_{\mathcal{H}} r \frac{df(r, h)}{dt} dr dh}{\int_{\mathcal{R}} \int_{\mathcal{H}} f(r, h) dr dh} \quad (26)$$

511
512
513 Figure 10 shows the spatial distribution of the representative floe radius in winter and
514 summer for all experiments with the prognostic FSD. As described in section 3, $L(r, h)$ is
515 initialized by the power law distribution with the exponent as 2.1 for all experiments. Exp-
516 WaveFrac-P shows smaller floe radius in the Chukchi and East Siberian Seas and north of
517 Greenland at the early stage of simulation compared to experiments using PF1 formulation (Fig.
518 10a₁-c₁, upper panel). Small-floe areas in Exp-WaveFrac-P are mostly contributed by the effect
519 of wave-fracturing where decreasing tendency of floe radius can extend further into the central
520 Arctic from the Atlantic and the Bering Strait compared to PF1 experiments (Fig. S6). After
521 September, 2016, the representative floe radii of PF experiments emerge, that is, Exp-
522 WaveFrac-P has smaller floe size compared to PF1 experiments for both winter and summer
523 (Fig. 10a-c). In summer, Exp-WaveFrac-P shows mostly fully-fractured floe (<10m, Fig. 10c,
524 bottom panel). The stronger wave-fracturing shown in Exp-WaveFrac-P is partly contributed
525 by the semi-empirical wave spectrum used in PF2. The simulated wave parameters under ice-
526 covered area are mostly with $H_s < 0.01$ m/s and $T_p > 15$ s. The constructed wave spectrum
527 and amplitude based on simulated wave parameters under sea ice and equations (17) and (18)
528 still include the contribution from high-frequency waves ($T = 2s$ bin), especially in the ice
529 pack far from the ice edge. The high-frequency waves only account for small fraction in the
530 wave period distribution $\bar{P}(T)$, and have small wave amplitude $A(T)$ ($\sim 7 \times 10^{-4}m$). The



531 strain of high-frequency bin based on equation (20) still exceeds the yielding strain and then
532 fractures floe into the smallest floe size category. Observational and numerical studies showed
533 that high-frequency waves rapidly decay and reach “zero” transmission state for high-
534 frequency waves when traveling under sea ice (e.g., Collins et al., 2015; Liu et al., 2020).
535 Despite the over-fracturing behavior shown in Exp-WaveFrac-P, the prevalence of small-floe
536 does not translate into the stronger ocean-induced ice melt but weaker melt in summer
537 compared to Exp-PFSD (Fig. 3d-e, Fig. S7e), indicating the limiting role of melting potential.
538 The weaker ocean-induced ice melt in summer of Exp-WaveFrac-P is corresponded to smaller
539 ice-ocean heat fluxes (Fig. S8a), which is contributed by both smaller friction velocity and
540 temperature difference (Fig. S8b-c).

541 **4.4 Sensitivity to wave-attenuation parameterization**

542 We have shown that ocean waves can alter the upper ocean through wave-enhanced
543 mixing, which may affect sea ice locally (Fig. 8, see section 4.1). The results from PF1 and
544 PF2 experiments imply that the simulated wave parameters can determine how ice floes are
545 fractured. As described in section 2.1, we can choose different coefficients in equation (2) to
546 control the wave attenuation rate of each frequency. In this section, we conduct experiments
547 using R18 coefficients (see section 3 and Table 2) to study the impacts of wave-attenuation rate
548 on Arctic sea ice simulation. The simulated sea ice area in Exp-WaveAtt-C (Fig. 2d, light-blue
549 line) resembles that in Exp-CFSD (Fig. 2d, blue line) before 2019. After 2019, Exp-WaveAtt-
550 C simulates smaller ice area compared to Exp-CFSD. Since both Exp-CFSD and Exp-WaveAtt-
551 C use constant floe size, which allows us to neglect the effect of spatial distribution of floe size



552 and MP87 lateral melting rate, which make lateral melt have negligible contribution (Fig. S9d),
553 basal melt is the primary factor for the ocean-induced ice melt during the entire period (Fig. 3a,
554 3f, and Fig. S9e). The strength of basal melt in Exp-WaveAtt-C is weaker than that in Exp-
555 CFSD from April, 2018 to January, 2020 (Fig. S9c). Basal growth of Exp-WaveAtt-C is also
556 smaller than that of Exp-CFSD in the winter of 2018 and 2019 (Fig. S9f). Compared to Exp-
557 CFSD, Exp-WaveAtt-C shows stronger top melt in summer of 2018 (Fig. S9b). The combined
558 effects of above processes lead to thinner ice state in Exp-WaveAtt-C before 2019 (Fig. S9a).
559 The thinner state of Exp-WaveAtt-C in the winter of 2019 make more open-water be created
560 by basal melt (regardless of its smaller magnitude) and thus smaller SIA (Fig. 2d), which is
561 also shown in the thermally-induced ice area changes that Exp-WaveAtt-C has smaller
562 magnitude in the corresponded period (Fig. 6d). As discussed in section 4.1, top melt and basal
563 growth is in good agreement with the ice-atmosphere heat flux (Fig. S9, S10a). That is, ice
564 mass and area changes described above are mainly driven by the ice-atmosphere heat flux
565 associated with the atmospheric responses to the changes in ocean wave conditions.

566 Different from the M14 experiments, the simulated sea ice area of Exp-WaveAtt-C (light-
567 blue line) and Exp-WaveAtt-P (yellow line) show relatively similar evolution during 2016-
568 2020 (Fig. 2d). The R18 coefficients represent weaker wave attenuation relative to the M14
569 coefficients. Thus, ocean waves in the R18 experiments are expected to transmit further into
570 the ice pack while maintaining relatively higher wave energy. To quantify to what extent the
571 ice can be affected by wave, we calculate the wave-affected extent (WAE), which is defined as
572 the sum of the area of cells with ice concentration greater than 15% and significant wave height



573 greater than 30cm (Cooper et al., 2022). Figure 11 shows the evolution of WAE for the M14
574 and R18 experiments with 15-day running average to smooth the high-frequency changes of
575 wave conditions. The weaker attenuation in Exp-WaveAtt-C and Exp-WaveAtt-P results in
576 generally larger WAE compared to Exp-CFSD and Exp-PFSD (as well as all previous
577 experiments with M14 coefficients, not shown). The direct impact of larger WAE in Exp-
578 WaveAtt-P is that the representative floe radius is mostly smaller than 10m (fully-fractured by
579 waves) (Fig. 10d). The decreasing tendency of floe radius due to wave-fracturing is the
580 dominant factor contributed to the fully-fractured condition (Fig. S6). Similar to Exp-
581 WaveFrac-P, the fully-fractured condition does not lead to stronger ocean-induced melt due to
582 limited oceanic energy (Fig. 3b, 3e, 3g, S9e).

583 **5. Conclusions and Discussions**

584 This study investigates the impacts of ocean waves on Arctic sea ice simulation based on
585 a newly-developed atmosphere-ocean-wave-sea ice coupled model, which is built on the
586 Coupled Arctic Prediction System (CAPS) by coupling the Simulating Waves Nearshore
587 (SWAN) and the implementation of the modified joint floe size and thickness distribution
588 (FSTD). A set of pan-Arctic experiments with different configurations of FSD-related
589 processes are performed for the period 2016-2020. Specifically, we examine the contrasting
590 behaviors of sea ice between constant and prognostic floe size, the responses of sea ice to
591 different lateral melting rate formulations, and the sensitivity of sea ice to the simulated wave
592 parameters under the atmosphere-ocean-wave-sea ice coupled framework.

593 The results of FSD-fixed and FSD-varied experiments show that the simulated sea ice



594 area is generally lower with smaller floe size associated with physical processes that change
595 FSD. According to sea ice mass budget analysis, smaller floe size contributes to increased
596 lateral melt, but its effect is reduced by decreased basal melt. The combined effects of lateral
597 and basal melt associated with smaller floe size result in relatively more ice melt by the ocean
598 energy, which is similar to previous studies (e.g., Bateson et al., 2022; Roach et al., 2019; Smith
599 et al., 2022). The simulations in Smith et al. (2022) with varying lateral melting strength based
600 on the Community Earth System Model version 2 (CESM2) with a slab-ocean model showed
601 minimal change in frazil ice formation. In our simulation with a full ocean model, the enhanced
602 ice melt by the ocean, though it is partially balanced by increased frazil ice formation due to
603 the depletion of melting potential in the surface layer. This suggests negative feedback from
604 the full ocean physics. Our fully-coupled simulations also show that atmospheric states respond
605 to changing ice distributions and then modify the energy budget at the ice surface that
606 determines top melt in summer and basal growth in winter. The FSD-varied experiments, in
607 general, show more energy loss from ice to atmosphere in winter, and all experiments show
608 year-to-year variations of energy gain for sea ice in summer.

609 The depletion of ocean energy in the surface layer as well as enhanced frazil ice formation
610 are the direct responses to the changes of ice-ocean coupling with the prognostic FSD. The
611 fractured sea ice enlarges the ice-ocean heat flux while the freezing temperature is still
612 determined by the sea surface salinity in the ocean model. However, the local salinity at the
613 ice-ocean interface can be significantly lower than sea surface salinity, and thus higher freezing
614 temperature locally due to the meltwater from sea ice (e.g., the false-bottom, Notz et al., 2003).



615 Schmidt et al. (2004) proposed the ice-ocean heat flux formulation that considers the local
616 salinity equilibrium but its formulation is only for the ice bottom interface. The generalization
617 of ice-ocean heat flux with the consideration of local salinity equilibrium for both bottom and
618 lateral interface might yield a more realistic ice-ocean coupled simulation. Although the lateral
619 melting rate formulation does not have the major effect on the simulated floe size distribution,
620 the simulated sea ice area and ice mass budget are sensitive to the choice of the formulation.
621 The lateral melting rate formulations applied in this study as well as previous laboratory results
622 are not related the ice properties (i.e., ice thickness and floe size, Josberger and Martin, 1981;
623 Maykut and Perovich, 1987; Perovich, 1983). A recent laboratory study suggested that the
624 lateral melting rate is a function of temperature difference and the ratio of floe size to ice
625 thickness (Li et al., 2021). Smith et al. (2022) also suggested that Arctic sea ice simulation can
626 be sensitive to the lateral melting rate of Perovich (1983) with different weights on each ice
627 thickness category. Further studies are required to investigate improved lateral melting rate
628 parameterization with observational constraints (e.g., data from the MOSAiC campaign in
629 2020, Nicolaus et al., 2021) within the prognostic FSD framework.

630 As discussed in Horvat and Tziperman (2015), the FTSD is sensitive to the wave
631 attenuation coefficients. Our simulations also show substantially contrasting behaviors in the
632 simulated floe size distribution associated with simulated wave parameters, suggesting that
633 several aspects need further investigation. First, the empirical wave attenuation (i.e., IC4M2)
634 may have reasonable performance in simulating the changes of wave energy spectrum locally
635 with specific ice conditions (e.g., Liu et al., 2020). However, the dissipation of wave energy



636 varies spatially for the pan-Arctic (as well as pan-Antarctic) scale simulation with the different
637 sea ice properties (i.e., ice concentration, ice thickness, floe size). Thus, a viscous boundary
638 layer model (Liu et al., 1991) or a viscoelastic model (Wang and Shen, 2010) for wave
639 attenuation, which provides spatially-varied wave attenuation with respect to sea ice properties,
640 might be able to give more realistic simulations in the wave-fracturing process and thus the
641 floe size distribution. Also, the current implementation of sea ice effects in the SWAN model
642 does not include the reflection and scattering due to sea ice, which redistributes the wave energy
643 spatially and potentially changes the wave-fracturing behavior. Second, the probability of floe-
644 fracturing $Q(r)$ in both formulations applied in this study are uncertain. Both formulations
645 result in floe-fracturing into smaller floe size categories within a short time-interval as long as
646 the simulated wave parameters satisfying the yielding strain. This strong contribution in the
647 wave-fracturing term is not easily balanced by the floe-welding term. The floe-welding term
648 (Roach et al., 2018a, b) acts to reduce the floe number density so that it is less effective in
649 increasing the representative floe radius if the floe is mostly fractured with the smallest floe
650 size. Third, the attenuated wave energy by sea ice does not influence sea ice conditions in this
651 study. As suggested by Longuet-Higgins and Steward (1962), the attenuated wave energy is
652 transferred into the ocean (as we described in section 3 for wave-enhanced mixing) or sea ice.
653 For sea ice, the transferred energy acts as a stress, called wave radiation stress (WRS), pushing
654 sea ice to the direction of wave propagation. By including the WRS in the momentum equation
655 of ice, the WRS then can affect sea ice drift (e.g., Boutin et al., 2020).

656 For quantitative applications (e.g., forecasting sea ice), more observations (especially



657 ocean waves under sea ice and FSD) are needed to reduce uncertainties in the atmosphere-
658 ocean-wave-sea ice coupled model, particular wave-related processes in ice-covered regions.
659 Horvat et al. (2019) developed a new technique to retrieve pan-Arctic scale FSD climatology
660 and seasonal cycle from CryoSat-2 radar altimeter and this method can resolve floe size from
661 300 m to 100 km and potentially up to 20 m scale if applying to ICESat-2 data. ICESat-2
662 altimetry also provides a new opportunity to observe ocean waves in sea ice at hemispheric-
663 scale coverage by directly observing the vertical displacements of the ice surface (e.g., Horvat
664 et al., 2020). In situ observations, despite their limited spatial coverage, are valuable wave
665 spectra measurements for wave-physics validation and improvement (e.g., Cooper et al., 2022;
666 Liu et al., 2020).
667



668 Code and data availability: The outputs of pan-Arctic simulation analyzed in this study
669 are archived in <https://doi.org/10.5281/zenodo.7922725>.

670

671 Author contributions: CYY and JL designed the model experiments, developed the
672 updated CAPS model, and wrote the manuscript, CYY conducted the experiments and analyzed
673 the results. DC provided constructive feedback on the manuscript.

674

675 Competing interests: The authors declare that they have no conflict of interest.

676

677 Acknowledgements: This research is supported by the National Natural Science
678 Foundation of China (42006188), the National Key R&D Program of China
679 (2018YFA0605901), and the Innovation Group Project of Southern Marine Science and
680 Engineering Guangdong Laboratory (Zhuhai) (311021008).

681



682 **6. References**

- 683 Asplin, M. G., Scharien, R., Else, B., Howell, S., Barber, D. G., Papakyriakou, T., and
684 Prinsenberg, S.: Implications of fractured Arctic perennial ice cover on thermodynamic
685 and dynamic sea ice processes, *J. Geophys. Res. Oceans*, 119, 2327–2343,
686 <https://doi.org/10.1002/2013JC009557>, 2014.
- 687 Bai, Q., and Bai, Y.: 7 - Hydrodynamics around Pipes, *Subsea Pipeline Design, Analysis, and*
688 *Installation*, Gulf Professional Publishing, 153-170, [https://doi.org/10.1016/B978-0-12-](https://doi.org/10.1016/B978-0-12-386888-6.00007-9)
689 [386888-6.00007-9](https://doi.org/10.1016/B978-0-12-386888-6.00007-9), 2014.
- 690 Bateson, A. W., Feltham, D. L., Schröder, D., Hosekova, L., Ridley, J. K., and Aksenov, Y.:
691 Impact of sea ice floe size distribution on seasonal fragmentation and melt of Arctic sea
692 ice, *The Cryosphere*, 14, 403–428, <https://doi.org/10.5194/tc-14-403-2020>, 2020.
- 693 Bateson, A. W., Feltham, D. L., Schröder, D., Wang, Y., Hwang, B., Ridley, J. K., and Aksenov,
694 Y.: Sea ice floe size: its impact on pan-Arctic and local ice mass and required model
695 complexity, *The Cryosphere*, 16, 2565–2593, <https://doi.org/10.5194/tc-16-2565-2022>,
696 2022.
- 697 Battjes, J. A. and Janssen, J. P. F. M.: Energy loss and set-up due to breaking of random waves,
698 *Proc. 16th Int. Conf. Coastal Engineering*, ASCE, 569-587,
699 <https://doi.org/10.1061/9780872621909.034>, 1978.
- 700 Bennetts, L. G., O'Farrell, S., and Uotila, P.: Brief communication: Impacts of ocean-wave-
701 induced breakup of Antarctic sea ice via thermodynamics in a stand-alone version of the
702 CICE sea-ice model, *The Cryosphere*, 11, 1035–1040, [https://doi.org/10.5194/tc-11-1035-](https://doi.org/10.5194/tc-11-1035-2017)
703 [2017](https://doi.org/10.5194/tc-11-1035-2017), 2017.
- 704 Bitz, C. M. and Lipscomb, W. H.: An energy-conserving thermodynamic sea ice model for
705 climate study. *J. Geophys. Res.-Oceans*, 104, 15669–15677,
706 <https://doi.org/10.1029/1999JC900100>, 1999.



-
- 707 Blanchard-Wrigglesworth, E., Donohoe, A., Roach, L. A., DuVivier, A., and Bitz, C. M.: High-
708 frequency sea ice variability in observations and models. *Geophysical Research Letters*,
709 48, e2020GL092356. <https://doi.org/10.1029/2020GL092356>, 2021.
- 710 Booij, N., Ris, R. C., and Holthuijsen, L. H.: A third-generation wave model for coastal regions.
711 Part I: Model description and validation. *Journal of Geophysical Research* 104 (C4),
712 7649–7666, <https://doi.org/10.1029/98JC02622>, 1999.
- 713 Boutin, G., Lique, C., Ardhuin, F., Rousset, C., Talandier, C., Accensi, M., and Girard-Ardhuin,
714 F.: Towards a coupled model to investigate wave–sea ice interactions in the Arctic
715 marginal ice zone, *The Cryosphere*, 14, 709–735, <https://doi.org/10.5194/tc-14-709-2020>,
716 2020.
- 717 Bretschneider, C. L.: Wave variability and wave spectra for wind-generated gravity waves,
718 1959.
- 719 Briegleb, B. P. and Light, B.: A Delta-Eddington multiple scattering parameterization for solar
720 radiation in the sea ice component of the Community Climate System Model. (No.
721 NCAR/TN-472+STR). University Corporation for Atmospheric Research,
722 <https://doi.org/10.5065/D6B27S71>, 2007.
- 723 Casas-Prat, M., and Wang, X.: Sea ice retreat contributes to projected increases in extreme
724 Arctic ocean surface waves. *Geophysical Research Letters*, 47, e2020GL088100.
725 <https://doi.org/10.1029/2020GL088100>, 2020.
- 726 Cassano, J. J., Higgins, M. E., and Seefeldt, M. W.: Performance of the Weather Research and
727 Forecasting Model for Month-Long Pan-Arctic Simulations. *Monthly Weather Review*,
728 139, 11, 3469–3488, <https://doi.org/10.1175/MWR-D-10-05065.1>, 2011.
- 729 Cavalieri, D. J., Parkinson, C. L., Gloersen, P., and Zwally, H. J.: updated yearly. Sea Ice
730 Concentrations from Nimbus-7 SMMR and DMSP SSM/I-SSMIS Passive Microwave
731 Data, Version 1. Boulder, Colorado USA. NASA National Snow and Ice Data Center
732 Distributed Active Archive Center. <https://doi.org/10.5067/8GQ8LZQVL0VL>, 1996.



-
- 733 Chen, F. and Dudhia, J.: Coupling an advanced land surface–hydrology model with the Penn
734 State–NCAR MM5 modeling system. Part I: Model implementation and sensitivity. *Mon.*
735 *Wea. Rev.*, 129, 569–585, [https://doi.org/10.1175/1520-](https://doi.org/10.1175/1520-0493(2001)129<0569:CAALSH>2.0.CO;2)
736 [0493\(2001\)129<0569:CAALSH>2.0.CO;2](https://doi.org/10.1175/1520-0493(2001)129<0569:CAALSH>2.0.CO;2), 2001.
- 737 Cole, S. T., Toole, J. M., Lele, R., Timmermans, M.-L., Gallagher, S. G., Stanton, T. P., Shaw,
738 W. J., Hwang, B., Maksym, T., Wilkinson, J. P., Ortiz, M., Graber, H., Rainville, L., Petty,
739 A. A., Farrell, S. L., Richter-Menge, J. A., and Haas, C.: Ice and ocean velocity in the
740 Arctic marginal ice zone: Ice roughness and momentum transfer, *Elementa: Science of the*
741 *Anthropocene*, 5, 55, <https://doi.org/10.1525/elementa.241>, 2017.
- 742 Collins, C. O., III, Rogers, W. E., Marchenko, A., and Babanin, A. V.: In situ measurements of
743 an energetic wave event in the Arctic marginal ice zone, *Geophys. Res. Lett.*, 42, 1863–
744 1870, <https://doi.org/10.1002/2015GL063063>, 2015.
- 745 Collins, C. O., and Rogers, W. E.: A Source Term for Wave Attenuation by Sea ice in
746 WAVEWATCH III: IC4, NRL Report NRL/MR/7320–17-9726, 25pp. Available from
747 <https://www7320.nrlssc.navy.mil/pubs.php>, 2017.
- 748 Collins, W. D., Rasch, P. J., Boville, B. A., McCaa, J., Williamson, D. L., Kiehl, J. T., Briegleb,
749 B. P., Bitz, C., Lin, S.-J., Zhang, M., and Dai, Y.: Description of the NCAR Community
750 Atmosphere Model (CAM 3.0). (No. NCAR/TN-464+STR). University Corporation for
751 Atmospheric Research. <https://doi.org/10.5065/D63N21CH>, 2004.
- 752 Cooper, V. T., Roach, L. A., Thomson, J., Brenner, S. D., Smith, M. M., Meylan, M. H., and
753 Bitz, C.M.: Wind waves in sea ice of the western Arctic and a global coupled wave-ice
754 model. *Phil. Trans. R. Soc. A.*, 380, 20210258, <https://doi.org/10.1098/rsta.2021.0258>,
755 2022.
- 756 Curry, J. A., Schramm, J. L., and Ebert, E. E.: Sea ice-albedo climate feedback mechanism, *J.*
757 *Climate*, 8, 240–247, [https://doi.org/10.1175/1520-](https://doi.org/10.1175/1520-0442(1995)008<0240:SIACFM>2.0.CO;2)
758 [0442\(1995\)008<0240:SIACFM>2.0.CO;2](https://doi.org/10.1175/1520-0442(1995)008<0240:SIACFM>2.0.CO;2), 1995.



-
- 759 Dobrynin, M., Murawsky, J., and Yang, S.: Evolution of the global wind wave climate in
760 CMIP5 experiments, *Geophys. Res. Lett.*, 39, L18606,
761 <https://doi.org/10.1029/2012GL052843>, 2012.
- 762 Dumont, D., Kohout, A., and Bertino, L.: A wave-based model for the marginal ice zone
763 including a floe breaking parameterization, *J. Geophys. Res.*, 116, C04001,
764 <https://doi.org/10.1029/2010JC006682>, 2011.
- 765 Freitas, S. R., Grell, G. A., Molod, A., Thompson, M. A., Putman, W. M., Santos e Silva, C. M.
766 and Souza, E. P.: Assessing the Grell–Freitas convection parameterization in the NASA
767 GEOS modeling system. *J. Adv. Model. Earth Syst.*, 10, 1266–1289,
768 <https://doi.org/10.1029/2017MS001251>, 2018.
- 769 Gupta, M., and Thompson, A. F.: Regimes of sea-ice floe melt: Ice-ocean coupling at the
770 submesoscales. *Journal of Geophysical Research: Oceans*, 127, e2022JC018894.
771 <https://doi.org/10.1029/2022JC018894>, 2022.
- 772 Hasselmann, S., Hasselmann, K., Allender, J. H., and Barnett, T. P.: Computations and
773 parameterizations of the nonlinear energy transfer in a gravity wave spectrum. Part II:
774 Parameterizations of the nonlinear transfer for application in wave models, *J. Phys.*
775 *Oceanogr.*, 15, 11, 1378-1391, [https://doi.org/10.1175/1520-0485\(1985\)015<1378:CAPOTN>2.0.CO;2](https://doi.org/10.1175/1520-0485(1985)015<1378:CAPOTN>2.0.CO;2), 1985.
- 777 Horvat, C.: Marginal ice zone fraction benchmarks sea ice climate model skill, *Nature*
778 *communications*, 12, 2221, <https://doi.org/10.1038/s41467-021-22004-7>, 2021.
- 779 Horvat, C., Blanchard-Wrigglesworth, E., and Petty, A. A.: Observing waves in sea ice with
780 ICESat-2. *Geophysical Research Letters*, 47, e2020GL087629.
781 <https://doi.org/10.1029/2020GL087629>, 2020.
- 782 Horvat, C. and Tziperman, E.: A prognostic model of the sea-ice floe size and thickness
783 distribution, *The Cryosphere*, 9, 2119–2134, <https://doi.org/10.5194/tc-9-2119-2015>,
784 2015.



-
- 785 Horvat, C., Tziperman, E., and Campin, J.-M.: Interaction of sea ice floe size, ocean eddies,
786 and sea ice melting, *Geophys. Res. Lett.*, 43, 8083-8090,
787 <https://doi.org/10.1002/2016GL069742>, 2016.
- 788 Horvat, C., Roach, L. A., Tilling, R., Bitz, C. M., Fox-Kemper, B., Guider, C., Hill, K., Ridout,
789 A., and Shepherd, A.: Estimating the sea ice floe size distribution using satellite altimetry:
790 theory, climatology, and model comparison, *The Cryosphere*, 13, 2869-2885,
791 <https://doi.org/10.5194/tc-13-2869-2019>, 2019.
- 792 Hunke, E. C. and Dukowicz, J. K.: An elastic-viscous-plastic model for sea ice dynamics. *J.*
793 *Phys. Oceanogr.* 27, 1849–67, [https://doi.org/10.1175/1520-](https://doi.org/10.1175/1520-0485(1997)027<1849:AEVPMF>2.0.CO;2)
794 [0485\(1997\)027<1849:AEVPMF>2.0.CO;2](https://doi.org/10.1175/1520-0485(1997)027<1849:AEVPMF>2.0.CO;2), 1997.
- 795 Josberger, E. G., and Martin, S.: A laboratory and theoretical study of the boundary layer
796 adjacent to a vertical melting ice wall in salt water. *J. Fluid Mech.*, 111, 439-473,
797 <https://doi.org/10.1017/S0022112081002450>, 1981.
- 798 Kirby, J. T., and Chen, T. M.: Surface waves on vertically sheared flows: approximate
799 dispersion relations. *J. Geophys. Res.*, 94, 1013-1027,
800 <https://doi.org/10.1029/JC094iC01p01013>, 1989.
- 801 Kohout, A., Williams, M. J., Dean, S. M., and Meylan, M.: Storm-induced sea-ice breakup and
802 the implications for ice extent. *Nature*, 509(7502), 604-607.
803 <https://doi.org/10.1038/nature13262>, 2014.
- 804 Komen, G. J., Hasselmann, S., and Hasselmann, K.: On the existence of a fully developed
805 wind-sea spectrum, *J. Phys. Oceanogr.*, 14, 1271-1285, [https://doi.org/10.1175/1520-](https://doi.org/10.1175/1520-0485(1984)014<1271:OTEQAF>2.0.CO;2)
806 [0485\(1984\)014<1271:OTEQAF>2.0.CO;2](https://doi.org/10.1175/1520-0485(1984)014<1271:OTEQAF>2.0.CO;2), 1984,
- 807 Kumar, N., Voulgaris, G., Warner, J. C., and Olabarrieta, M.: Implementation of the vortex
808 force formalism in the coupled ocean-atmosphere-wave-sediment transport (COAWST)
809 modeling system for inner shelf and surf zone applications, *Ocean Modelling*, 47, 65-95,
810 <https://doi.org/10.1016/j.ocemod.2012.01.003>, 2012.



-
- 811 Kwok, R.: Arctic sea ice thickness, volume, and multiyear ice coverage: Losses and coupled
812 variability (1958–2018), *Environ. Res. Lett.*, 13, 105005, [https://doi.org/10.1088/1748-](https://doi.org/10.1088/1748-9326/aae3ec)
813 [9326/aae3ec](https://doi.org/10.1088/1748-9326/aae3ec), 2018.
- 814 Langhorne, P. J., Squire, V. A., Fox, C., and Haskell, T. G.: Break-up of sea ice by ocean waves,
815 *Annals of Glaciology*, 27, 438–442. <https://doi.org/10.3189/S0260305500017869>, 1998.
- 816 Leonard, B., and Mokhtari, S.: ULTRA-SHARP Non oscillatory Convection Schemes for
817 High-Speed Steady Multidimensional Flow. Technical Report. NASA, 1990.
- 818 Li, Z., Wang, Z., Wang, Q., Xie, Fei., and Lu, P.: Laboratory study on parameterization of ice
819 floe melt rate at ice-air and ice-water interfaces. *Haiyang Xuebao*, 43(7), 162-172,
820 <https://doi.org/10.12284/hyxb2021115>, 2021. (in Chinese)
- 821 Liang, X., Losch, M., Nerger, L., Mu, L., Yang, Q., and Liu, C.: Using sea surface temperature
822 observations to constrain upper ocean properties in an Arctic sea ice-ocean data
823 assimilation system, *Journal of Geophysical Research: Oceans*, 124,
824 <https://doi.org/10.1029/2019JC015073>, 2019.
- 825 Lipscomb, W. H., Hunke, E. C., Maslowski, W., and Jakacki, J.: Ridging, strength, and stability
826 in high-resolution sea ice models. *J. Geophys. Res.*, 112, C03S91,
827 <https://doi.org/10.1029/2005JC003355>, 2007.
- 828 Liu, Q., Babanin, A. V., Zieger, S., Young, I. R., and Guan, C.: Wind and Wave Climate in the
829 Arctic Ocean as Observed by Altimeters. *Journal of Climate* 29, 22, 7957-7975,
830 <https://doi.org/10.1175/JCLI-D-16-0219.1>, 2016.
- 831 Longuet-Higgins, M. S. and Stewart, R. W.: Radiation stresses and mass transport in surface
832 gravity waves with application to ‘surf beats’, *J. Fluid Mech.*, 13, 481-504,
833 <https://doi.org/10.1017/S0022112062000877>, 1962.
- 834 Loose, B., McGillis, W. R., Perovich, D., Zappa, C. J., and Schlosser, P.: A parameter model of
835 gas exchange for the seasonal sea ice zone, *Ocean Sci.*, 10, 17-28,
836 <https://doi.org/10.5194/os-10-17-2014>, 2014.



-
- 837 Liu, A. K., Holt, B., and Vachon, P. W.: Wave propagation in the marginal ice zone: Model
838 predictions and comparisons with buoy and synthetic aperture radar data, *J. Geophys. Res.*,
839 96(C3), 4605-4621, <https://doi.org/10.1029/90JC02267>, 1991.
- 840 Liu, D., Tsarau, A., Guan, C., and Shen, H. H.: Comparison of ice and wind-wave modules in
841 WAVEWATCH III® in the Barents Sea, *Cold Regions Science and Technology*, 172,
842 103008, <https://doi.org/10.1016/j.coldregions.2020.103008>, 2020.
- 843 Lu, P., Li, Z., Cheng, B., and Leppäranta, M.: A parameterization of the ice-ocean drag
844 coefficient, *J. Geophys. Res.*, 116, C07019, <https://doi.org/10.1029/2010JC006878>, 2011.
- 845 Lukovich, J. V., Stroeve, J. C., Crawford, A., Hamilton, L., Tsamados, M., Heorton, H., and
846 Massonnet, F.: Summer Extreme Cyclone Impacts on Arctic Sea Ice, *Journal of Climate*,
847 34(12), 4817-4834, <https://doi.org/10.1175/JCLI-D-19-0925.1>, 2021.
- 848 Madsen, O. S., Poon, Y.-K., and Graber, H. C.: Spectral wave attenuation by bottom friction:
849 Theory, *Proc. 21th Int. Conf. Coastal Engineering, ASCE*, 492-504,
850 <https://doi.org/10.1061/9780872626874.035>, 1988.
- 851 Martin, T., Tsamados, M., Schroeder, D., and Feltham, D. L.: The impact of variable sea ice
852 roughness on changes in Arctic Ocean surface stress: A model study, *J. Geophys. Res.*
853 *Oceans*, 121, 1931– 1952, <https://doi.org/10.1002/2015JC011186>, 2016.
- 854 Maykut, G. A. and Perovich, D. K.: The role of shortwave radiation in the summer decay of a
855 sea ice cover, *J. Geophys. Res.-Ocean.*, 92, 7032–7044,
856 <https://doi.org/10.1029/JC092iC07p07032>, 1987.
- 857 Maykut, G. A. and McPhee, M. G.: Solar heating of the Arctic mixed layer, *J. Geophys. Res.-*
858 *Oceans*, 100, 24691–24703, <http://doi.org/10.1029/95JC02554>, 1995.
- 859 Meylan, M., and Squire, V. A.: The response of ice floes to ocean waves, *J. Geophys. Res.*,
860 99(C1), 891– 900, <https://doi.org/10.1029/93JC02695>, 1994.
- 861 Meylan, M. H., Bennetts, L. G., and A. L. Kohout: In situ measurements and analysis of ocean
862 waves in the Antarctic marginal ice zone, *Geophys. Res. Lett.*, 41, 1-6,
863 <https://doi.org/10.1002/2014GL060809>, 2014.



-
- 864 Montiel, F., Squire, V., and Bennetts, L.: Attenuation and directional spreading of ocean wave
865 spectra in the marginal ice zone. *Journal of Fluid Mechanics*, 790, 492-522.
866 <https://doi.org/10.1017/jfm.2016.21>, 2016.
- 867 Morrison, H., Thompson, G., and Tatarskii, V.: Impact of Cloud Microphysics on the
868 Development of Trailing Stratiform Precipitation in a Simulated Squall Line: Comparison
869 of One- and Two-Moment Schemes. *Mon. Wea. Rev.*, 137, 991-1007.
870 <https://doi.org/10.1175/2008MWR2556.1>, 2009.
- 871 Nakanishi, M., and Niino., H.: Development of an improved turbulence closure model for the
872 atmospheric boundary layer. *J. Meteor. Soc. Japan*, 87, 895-912,
873 <https://doi.org/10.2151/jmsj.87.895>, 2009.
- 874 Naughten, K. A., Galton-Fenzi, B. K., Meissner, K. J., England, M. H., Brassington, G. B.,
875 Colberg, F., Hattermann, T., and Debernard, J. B.: Spurious sea ice formation caused by
876 oscillatory ocean tracer advection schemes. *Ocean Model.*, 116, 108-117,
877 <https://doi.org/10.1016/j.ocemod.2017.06.010>, 2017.
- 878 Nicolaus, M., Perovich, D., Spreen, G., Granskog, M., Albedyll, L., Angelopoulos, M., Anhaus,
879 P., Arndt, S., Belter, H., Bessonov, V., Birnbaum, G., Brauchle, J., Calmer, R.,
880 Cardellach, E., Cheng, B., Clemens-Sewall, D., Dadic, R., Damm, E., Boer, G., Demir,
881 O., Dethloff, K., Divine, D., Fong, A., Fons, S., Frey, M., Fuchs, N., Gabarró, C.,
882 Gerland, S., Goessling, H., Gradinger, R., Haapala, J., Haas, C., Hamilton, J., Hannula,
883 H.-R., Hendricks, S., Herber, A., Heuzé, C., Hoppmann, M., Høyland, K., Huntemann,
884 M., Hutchings, J., Hwang, B., Itkin, P., Jacobi, H.-W., Jaggi, M., Jutila, A., Kaleschke,
885 L., Katlein, C., Kolabutin, N., Krampe, D., Kristensen, S., Krumpen, T., Kurtz, N.,
886 Lampert, A., Lange, B., Lei, R., Light, B., Linhardt, F., Liston, G., Loose, B., Macfarlane,
887 A., Mahmud, M., Matero, I., Maus, S., Morgenstern, A., Naderpour, R., Nandan, V.,
888 Niubom, A., Oggier, M., Oppelt, N., Pätzold, F., Perron, C., Petrovsky, T., Pirazzini, R.,
889 Polashenski, C., Rabe, B., Raphael, I., Regnery, J., Rex, M., Ricker, R., Riemann-Campe,
890 K., Rinke, A., Rohde, J., Salganik, E., Scharien, R., Schiller, M., Schneebeil, M.,



-
- 891 Semmling, M., Shimanchuk, E., Shupe, M., Smith, M., Smolyanitsky, V., Sokolov, V.,
892 Stanton, T., Stroeve, J., Thielke, L., Timofeeva, A., Tonboe, R., Tavri, A., Tsamados,
893 M., Wagner, D., Watkins, D., Webster, M., and Wendisch, M.: Overview of the
894 MOSAiC expedition – Snow and Sea Ice, *Elementa Science of the Anthropocene*,
895 <https://doi.org/10.1525/elementa.2021.000046>, 2021.
- 896 Notz, D., McPhee, M. G., Worster, M. G., Maykut, G. A., Schlünzen, K. H., and Eicken, H.:
897 Impact of underwater-ice evolution on Arctic summer sea ice, *J. Geophys. Res.-Oceans*,
898 108, 3223, <https://doi.org/10.1029/2001JC001173>, 2003.
- 899 Notz, D., Jahn, A., Holland, M., Hunke, E., Massonnet, F., Stroeve, J., Tremblay, B., and
900 Vancoppenolle, M.: The CMIP6 Sea-Ice Model Intercomparison Project (SIMIP):
901 understanding sea ice through climate-model simulations, *Geosci. Model Dev.*, 9, 3427-
902 3446, <https://doi.org/10.5194/gmd-9-3427-2016>, 2016.
- 903 Parkinson, C. L., and Comiso, J. C.: On the 2012 record low Arctic sea ice cover: Combined
904 impact of preconditioning and an August storm. *Geophysical Research Letters*, 40, 1356–
905 1361. <https://doi.org/10.1002/grl.50349>, 2013.
- 906 Peng, L., Zhang, X., Kim, J.-H., Cho, K.-H., Kim, B.-M., Wang, Z., and Tang, H.: Role of
907 intense Arctic storm in accelerating summer sea ice melt: An in situ observational study.
908 *Geophysical Research Letters*, 48, e2021GL092714.
909 <https://doi.org/10.1029/2021GL092714>, 2021.
- 910 Perovich, D.: On the summer decay of a sea ice cover, PhD thesis, University of Washington,
911 Seattle, 48–96, 1983.
- 912 Perovich, D., Meier, W., Tshudi, M., Hendricks, S., Petty, A. A., Divine, D., Farrell, S., Gerland,
913 S., Haas, C., Kaleschke, L., Pavlova, O., Ricker, R., Tian-Kunze, X., Webster, M., and
914 Wood, K.: Sea Ice, Arctic Report Card 2020, Thoman, R. L., Richter-Menge, J., and
915 Druckenmiller, M. L., Eds., <https://doi.org/10.25923/n170-9h57>, 2020.



-
- 916 Rampal, P., Weiss, J., and Marsan, D.: Positive trend in the mean speed and deformation rate
917 of Arctic sea ice, 1979–2007, *J. Geophys. Res.*, 114, C05013,
918 <https://doi.org/10.1029/2008JC005066>, 2009.
- 919 Roach, L. A., Horvat, C., Dean, S. M., and Bitz, C. M.: An emergent sea ice floe size
920 distribution in a global coupled ocean-sea ice model. *Journal of Geophysical Research:*
921 *Oceans*, 123, 4322–4337. <https://doi.org/10.1029/2017JC013692>, 2018a.
- 922 Roach, L. A., Smith, M. M., and Dean, S. M.: Quantifying growth of pancake sea ice floes
923 using images from drifting buoys. *Journal of Geophysical Research: Ocean*, 123, 2851-
924 2866. <https://doi.org/10.1002/2017JC013693>, 2018b.
- 925 Roach, L. A., Bitz, C. M., Horvat, C., and Dean, S. M.: Advances in Modeling Interactions
926 Between Sea Ice and Ocean Surface Waves, *J. Adv. Model. Earth Syst.*, 11, 4167-4181,
927 <https://doi.org/10.1029/2019MS001836>, 2019.
- 928 Rogers, W. E., Meylan, M. H., and Kohout, A. L.: Frequency Distribution of Dissipation of
929 Energy of Ocean Waves by Sea Ice Using Data from Wave Array 3 of the ONR "Sea State"
930 Field Experiment. *NRL Report NRL/MR/7322–18-9801.*, 25 pp, Available from
931 <https://www7320.nrlssc.navy.mil/pubs.php>, 2018.
- 932 Rogers, W. E.: Implementation of sea ice in the wave model SWAN, *NRL Memorandum Report*
933 *NRL/MR/7322–19-9874*, 25pp, Available from
934 <https://www7320.nrlssc.navy.mil/pubs.php>, 2019.
- 935 Rothrock, D. A. and Thorndike, A. S.: Measuring the sea ice floe size distribution, *J. Geophys.*
936 *Res.*, 89, 6477–6486, <https://doi.org/10.1029/JC089iC04p06477>, 1984.
- 937 Saha, S., Moorthi, S., Wu, X., Wang, J., Nadiga, S., Tripp, P., Behringer, D., Hou, Y., Chuang,
938 H., Iredell, M., Ek, M., Meng, J., Yang, R., Mendez, M. P., van den Dool, H., Zhang, Q.,
939 Wang, W., Chen, M., and Becker, E.: The NCEP climate forecast system version 2, *J.*
940 *Climate*, 27, 2185–2208, <https://doi.org/10.1175/JCLI-D-12-00823.1>, 2014.
- 941 Schäfer, M., Bierwirth, E., Ehrlich, A., Jäkel, E., and Wendisch, M.: Airborne observations and
942 simulations of three-dimensional radiative interactions between Arctic boundary layer



-
- 943 clouds and ice floes, *Atmos. Chem. Phys.*, 15, 8147-8163, [https://doi.org/10.5194/acp-15-](https://doi.org/10.5194/acp-15-8147-2015)
944 [8147-2015](https://doi.org/10.5194/acp-15-8147-2015), 2015.
- 945 Schmidt, G. A., Bitz, C. M., Mikolajewicz, U., and Tremblay, L.-B.: Ice–ocean boundary
946 conditions for coupled models, *Ocean Model.*, 7, 59-74, [https://doi.org/10.1016/S1463-](https://doi.org/10.1016/S1463-5003(03)00030-1)
947 [5003\(03\)00030-1](https://doi.org/10.1016/S1463-5003(03)00030-1), 2004.
- 948 Sepp, M., and Jaagus, J.: Changes in the activity and tracks of Arctic cyclones. *Climatic Change*,
949 105(3), 577–595. <https://doi.org/10.1007/s10584-010-9893-7>, 2011.
- 950 Shchepetkin, A. F., and McWilliams, J. C.: The Regional Ocean Modeling System: A split-
951 explicit, free-surface, topography following coordinates ocean model, *Ocean Modelling*,
952 9, 347-404, <https://doi.org/10.1016/j.ocemod.2004.08.002>, 2005.
- 953 Simmonds, I., and Rudeva, I.: The great Arctic cyclone of August 2012, *Geophys. Res. Lett.*,
954 39, L23709, <https://doi.org/10.1029/2012GL054259>, 2012.
- 955 Smith, M. M., Holland, M., and Light, B.: Arctic sea ice sensitivity to lateral melting
956 representation in a coupled climate model, *The Cryosphere*, 16, 419-434,
957 <https://doi.org/10.5194/tc-16-419-2022>, 2022.
- 958 Spreen, G., Kwok, R., and Menemenlis, D.: Trends in Arctic sea ice drift and role of wind
959 forcing: 1992–2009, *Geophys. Res. Lett.*, 38, L19501,
960 <https://doi.org/10.1029/2011GL048970>, 2011.
- 961 Squire, V. A.: Ocean Wave Interactions with Sea Ice: A Reappraisal, *Annual Review of Fluid*
962 *Mechanics*, 52:1, 37-60, <https://doi.org/10.1146/annurev-fluid-010719-060301>, 2020.
- 963 Squire, V. A., and Montiel, F.: Evolution of Directional Wave Spectra in the Marginal Ice Zone:
964 A New Model Tested with Legacy Data. *Journal of Physical Oceanography* 46, 10, 3121-
965 3137, <https://doi.org/10.1175/JPO-D-16-0118.1>, 2016.
- 966 Steele, M.: Sea ice melting and floe geometry in a simple ice-ocean model, *J. Geophys. Res.*,
967 97, 17-729-17738, <https://doi.org/10.1029/92JC01755>, 1992.



-
- 968 Steele, M., Morison, J. H., and Untersteiner, N.: The partition of air-ice-ocean momentum
969 exchange as a function of ice concentration, floe size, and draft, *J. Geophys. Res.*, 94(C9),
970 12739-12750, <https://doi.org/10.1029/JC094iC09p12739>, 1989.
- 971 Steer, A., Worby, A., and Heil, P.: Observed changes in sea-ice floe size distribution during
972 early summer in the western Weddell Sea, *Deep Sea Res., Part II*, 55, 933-942,
973 <https://doi.org/10.1016/j.dsr2.2007.12.016>, 2008.
- 974 Stern, D., P, Doyle, J. D., Barton, N. P., Finocchio, P. M., Komaromi, W. A., & Metzger, E. J.:
975 The impact of an intense cyclone on short-term sea ice loss in a fully coupled atmosphere-
976 ocean-ice model. *Geophysical Research Letters*, 47, e2019GL085580.
977 <https://doi.org/10.1029/2019GL085580>, 2020.
- 978 Stopa, J. E., Arduin, F., and Girard-Arduin, F.: Wave climate in the Arctic 1992-2014:
979 seasonality and trends, *The Cryosphere*, 10, 1605–1629, [https://doi.org/10.5194/tc-10-](https://doi.org/10.5194/tc-10-1605-2016)
980 1605-2016, 2016.
- 981 Taylor, P. K., and Yelland, M. J.: The dependence of sea surface roughness on the height and
982 steepness of the waves. *Journal of Physical Oceanography* 31, 572-590,
983 [https://doi.org/10.1175/1520-0485\(2001\)031<0572:TDOSSR>2.0.CO;2](https://doi.org/10.1175/1520-0485(2001)031<0572:TDOSSR>2.0.CO;2), 2001.
- 984 Thomson, J., and Rogers, W. E.: Swell and sea in the emerging Arctic Ocean, *Geophys. Res.*
985 *Lett.*, 41, 3136–3140, <https://doi.org/10.1002/2014GL059983>, 2014.
- 986 Thorndike, A. S., Rothrock, D. A., Maykut, G. A., and Colony, R.: The thickness distribution
987 of sea ice, *J. Geophys. Res.*, 80, 4501, <https://doi.org/10.1029/JC080i033p04501>, 1975.
- 988 Toyota, T., Takatsuji, S., and Nakayama, M.: Characteristics of sea ice floe size distribution in
989 the seasonal ice zone, *Geophys. Res. Lett.*, 33, L02616,
990 <https://doi.org/10.1029/2005GL024556>, 2006.
- 991 Toyota, T., Haas, C., and Tamura, T.: Size distribution and shape properties of relatively small
992 sea-ice floes in the Antarctic marginal ice zone in late winter, *Deep Sea Res., Part II*, 58,
993 1182–1193, <https://doi.org/10.1016/j.dsr2.2010.10.034>, 2011.



-
- 994 Tschudi, M. A., Stroeve, J. C., and Stewart, J. S.: Relating the age of Arctic sea ice to its
995 thickness, as measured during NASA's ICESat and IceBridge campaigns. *Remote Sensing*,
996 8(6), 457, 2016.
- 997 Tsamados, M., Feltham, D. L., Schroeder, D., Flocco, D., Farrell, S. L., Kurtz, N., Laxon, S.
998 W., and Bacon, S.: Impact of Variable Atmospheric and Oceanic Form Drag on
999 Simulations of Arctic Sea Ice. *Journal of Physical Oceanography* 44, 5, 1329-1353,
1000 <https://doi.org/10.1175/JPO-D-13-0215.1>, 2014.
- 1001 Tsamados, M., Feltham, D., Petty, A., Schroeder, D., Flocco, D.: Processes controlling surface,
1002 bottom and lateral melt of Arctic sea ice in a state of the art sea ice model. *Phil. Trans. R.*
1003 *Soc. A*, 373: 20140167. <https://doi.org/10.1098/rsta.2014.0167>, 2015.
- 1004 Uchiyama, Y., McWilliams, J. C., and Shepetchkin, A. F.: Wave-current interaction in an
1005 oceanic circulation model with a vortex-force formalism: Application to the surf zone,
1006 *Ocean Modelling*, 34, 1-2, 16-35, <https://doi.org/10.1016/j.ocemod.2010.04.002>, 2010.
- 1007 Umlauf, L. and Burchard, H.: A generic length-scale equation for geophysical turbulence
1008 models, *J. Marine Res.*, 61, 235-265, <https://doi.org/10.1357/002224003322005087>, 2003.
- 1009 Valkonen, E., Cassano, J., and Cassano, E.: Arctic cyclones and their interactions with the
1010 declining sea ice: A recent climatology. *Journal of Geophysical Research: Atmospheres*,
1011 126, e2020JD034366. <https://doi.org/10.1029/2020JD034366>, 2021.
- 1012 Vella, D., and Wettlaufer, J. S.: Explaining the patterns formed by ice floe interactions, *J.*
1013 *Geophys. Res.*, 113, C11011, <https://doi.org/10.1029/2008JC004781>, 2008.
- 1014 Wang, R., and Shen, H. H.: Gravity waves propagating into an ice-covered ocean: A
1015 viscoelastic model, *J. Geophys. Res.*, 115, C06024,
1016 <https://doi.org/10.1029/2009JC005591>, 2010.
- 1017 Warner, J. C., Armstrong, B., He, R., and Zambon, J.: Development of a coupled ocean-
1018 atmosphere-wave-sediment transport (COAWST) modeling system. *Ocean Modell.* 35,
1019 230–244, <https://doi.org/10.1016/j.ocemod.2010.07.010>, 2010.



-
- 1020 Waseda, T., Nose, T., Kodaira, T., Sasmal, K., and Webb, A.: Climatic trends of extreme wave
1021 events caused by Arctic cyclones in the western Arctic Ocean. *Polar Science*, 27, 100625.
1022 <https://doi.org/10.1016/j.polar.2020.100625>, 2021.
- 1023 Waseda, T., Webb, A., Sato, K., Inoue, J., Kohout, A., Penrose, B., and Penrose, S.: Correlated
1024 Increase of High Ocean Waves and Winds in the Ice-Free Waters of the Arctic Ocean. *Sci*
1025 *Rep* 8, 4489, <https://doi.org/10.1038/s41598-018-22500-9>, 2018.
- 1026 Weiss J. and Dansereau V.: Linking scales in sea ice mechanics. *Phil. Trans. R. Soc. A.*, 375,
1027 20150352, <http://doi.org/10.1098/rsta.2015.0352>, 2015.
- 1028 Wenta, M., Herman, A.: Area-Averaged Surface Moisture Flux over Fragmented Sea Ice: Floe
1029 Size Distribution Effects and the Associated Convection Structure within the Atmospheric
1030 Boundary Layer. *Atmosphere*, 10, 654. <https://doi.org/10.3390/atmos10110654>, 2019.
- 1031 Wilchinsky, A. V., Feltham, D. L., and Hopkins, M. A.: Effect of shear rupture on aggregate
1032 scale formation in sea ice, *J. Geophys. Res.*, 115, C10002,
1033 <https://doi.org/10.1029/2009JC006043>, 2010.
- 1034 Zahn, M., Akperov, M., Rinke, A., Feser, F., and Mokhov, I. I.: Trends of cyclone characteristics
1035 in the Arctic and their patterns from different reanalysis data. *Journal of Geophysical*
1036 *Research: Atmospheres*, 123, 2737–2751. <https://doi.org/10.1002/2017JD027439>, 2018.
- 1037 Zhang, F., Pang, X., Lei, R., Zhai, M., Zhao, X., and Cai, Q.: Arctic sea ice motion change and
1038 response to atmospheric forcing between 1979 and 2019. *International Journal of*
1039 *Climatology*, 42(3), 1854–1876. <https://doi.org/10.1002/joc.7340>, 2022
- 1040 Zhang, J., Lindsay, R., Schweiger, A., and Steele, M.: The impact of an intense summer cyclone
1041 on 2012 Arctic sea ice retreat. *Geophysical Research Letters*, 40, 720–726.
1042 <https://doi.org/10.1002/grl.50190>, 2013.
- 1043 Zhang, J., Schweiger, A., Steele, M., and Stern, H.: Sea ice floe size distribution in the marginal
1044 ice zone: Theory and numerical experiments, *J. Geophys. Res. Oceans*, 120,
1045 <https://doi.org/10.1002/2015JC010770>, 2015.



1046 Zhang, J., Stern, H., Hwang, B., Schweiger, A., Steele, M., Stark, M., Graber, H. C.: Modeling
1047 the seasonal evolution of the Arctic sea ice floe size distribution. *Elementa: Science of the*
1048 *Anthropocene*, 4, 000126, <https://doi.org/10.12952/journal.elementa.000126>, 2016.
1049



1050 **7. Tables**

1051 Table 1 The summary of physic parameterizations used in all pan-Arctic simulations.

WRF physics	
Cumulus	Grell-Freitas (Freitas et al. 2018)
Microphysics	Morrison 2-moment (Morrison et al. 2009)
Longwave radiation	CAM spectral band scheme (Collins et al. 2004)
Shortwave radiation	CAM spectral band scheme (Collins et al. 2004)
Boundary layer	MYNN (Nakanishi and Niino, 2009)
Land surface	Unified Noah LSM (Chen and Dudhia, 2001)
ROMS physics	
Tracer advection	Upwind third-order horizontal advection (U3H; Shchepetkin, and McWilliams, 2005) Centered fourth-order vertical advection (C4V; Shchepetkin, and McWilliams, 2005)
Tracer vertical mixing	Generic Length-Scale scheme (Umlauf and Burchard, 2003)
CICE physics	
Ice dynamics	EVP (Hunke and Dukowicz, 1997)
Ice thermodynamics	Bitz and Lipscomb (1999)
Shortwave albedo	Delta-Eddington (Briegleb and Light, 2007)
SWAN physics	
Exponential wind growth	Komen et al. (1984)
Whitecapping	Komen et al. (1984)
Quadruplets	Hasselmann et al. (1985)
Depth-induced breaking	Battjes and Janssen (1978)
Bottom friction	Madsen et al. (1988)
Sea ice dissipation	Collins and Rogers (2017); Rogers (2019)

1052

1053



1054 Table 2 The summary of the experiments conducted in this study and their main changes in the
1055 experiment design. MP87: Maykut and Perovich (1987). P83: Perovich (1983). M14: Meylan
1056 et al. (2014). R18: Rogers et al. (2018).

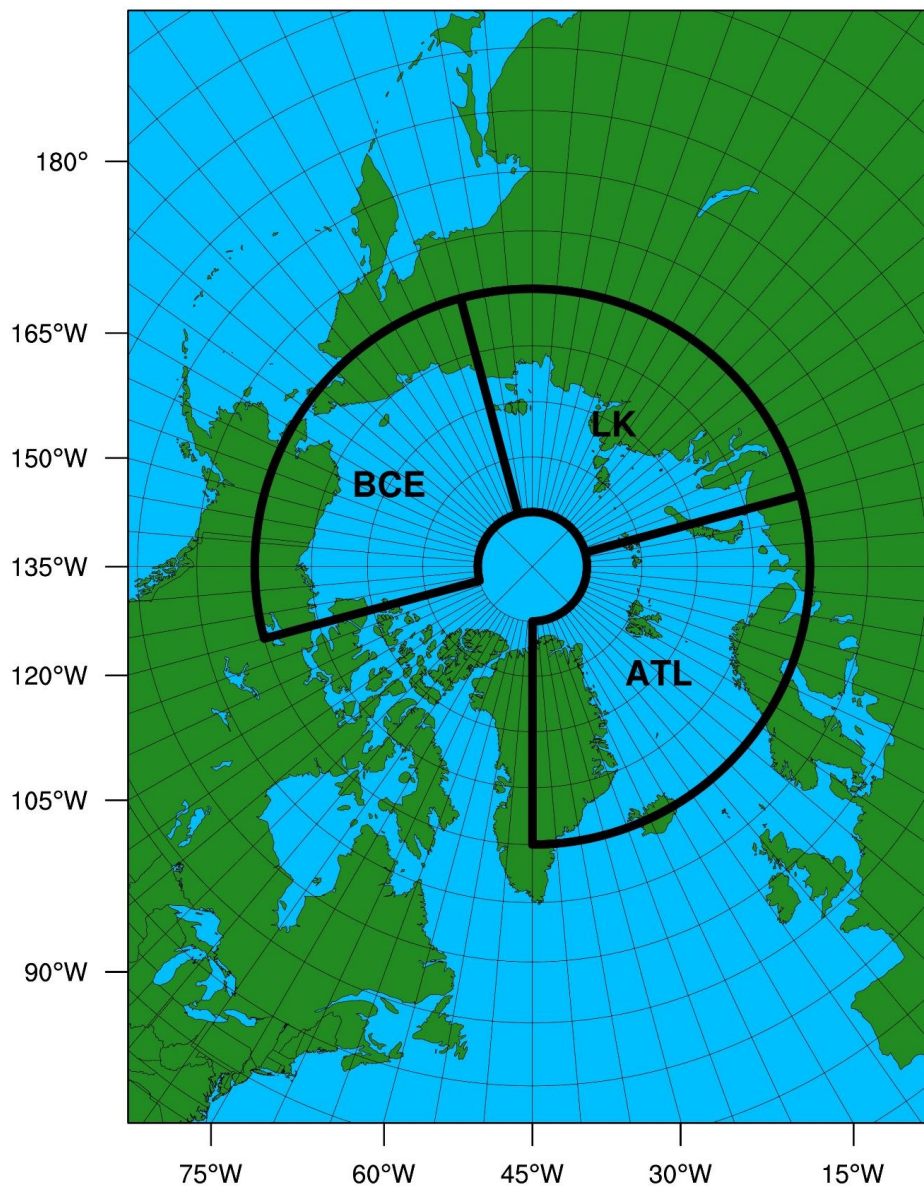
Experiment	Floe size	Lateral melting rate	Wave fracturing formulation	Wave attenuation coefficients
Exp-CFSD	Const. 300m	MP87	None	M14
Exp-PFSD	FSTD	MP87	Equally (PF1)	M14
Exp-LatMelt-C	Const. 300m	P83	None	M14
Exp-LatMelt-P	FSTD	P83	Equally (PF1)	M14
Exp-WaveFrac-P	FSTD	MP87	Bretschneider (PF2)	M14
Exp-WaveAtt-C	Const. 300m	MP87	None	R18
Exp-WaveAtt-P	FSTD	MP87	Equally (PF1)	R18

1057

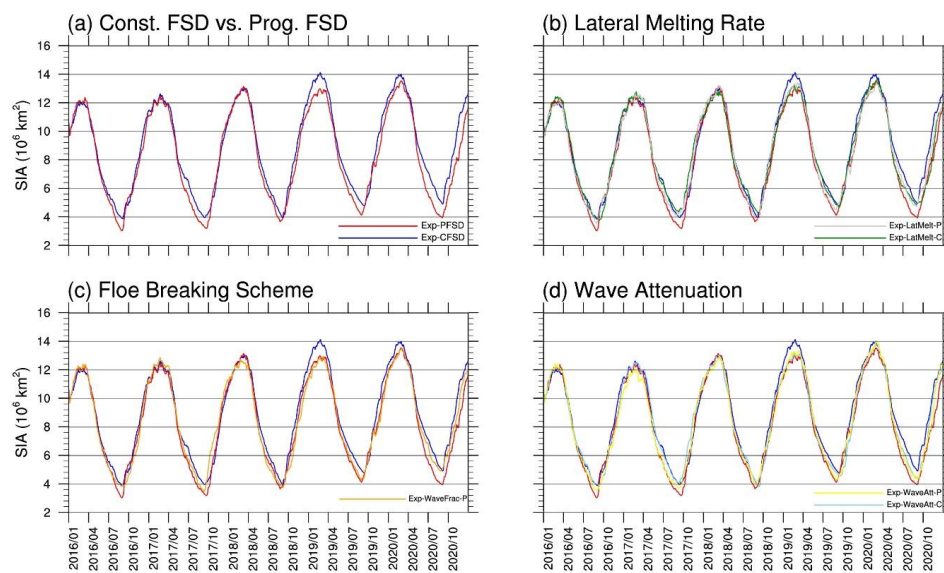
1058



1059 **8. Figures**



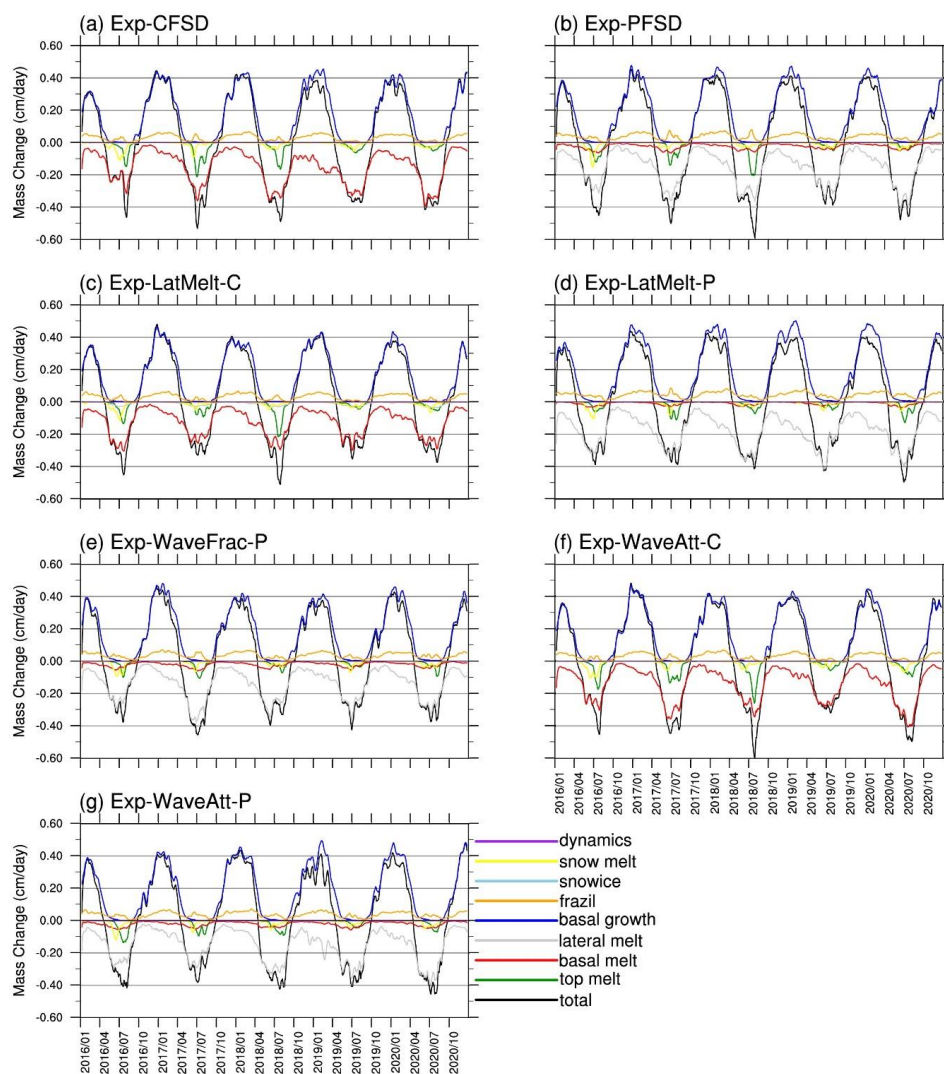
1060
1061 Figure 1 The model domain used in CAPS for pan-Arctic sea ice simulations. Black boxes
1062 indicate the subregions for analysis performed in this study.
1063



1064

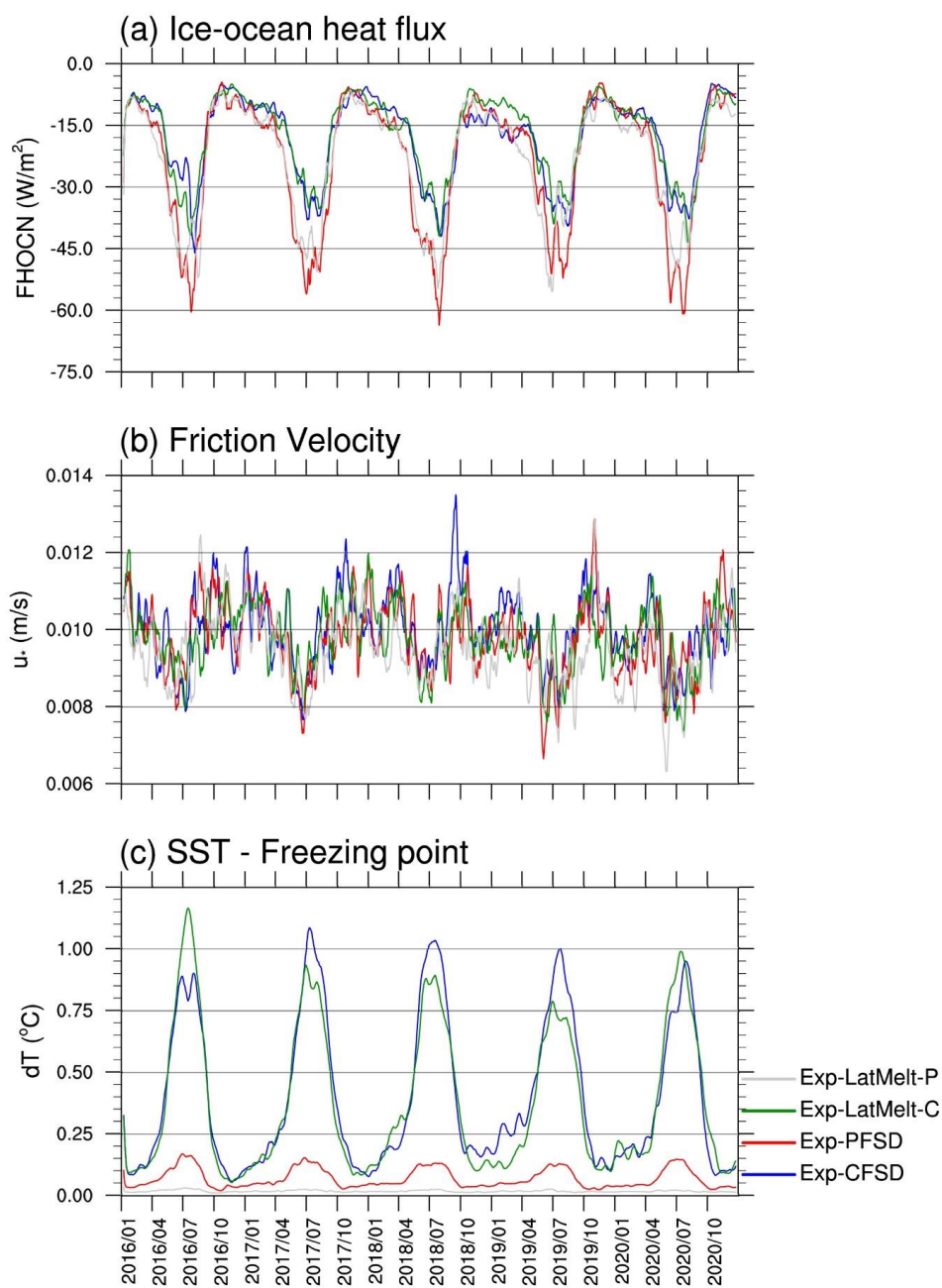
1065 Figure 2 Time-series of Arctic sea ice area for Exp-CFSD (blue line), Exp-PFSD (red line),
1066 Exp-LatMelt-C (green line), Exp-LatMelt-P (grey line), Exp-WaveFrac-P (orange line), Exp-
1067 WaveAtt-C (light-blue line) and Exp-WaveAtt-P (yellow line).

1068



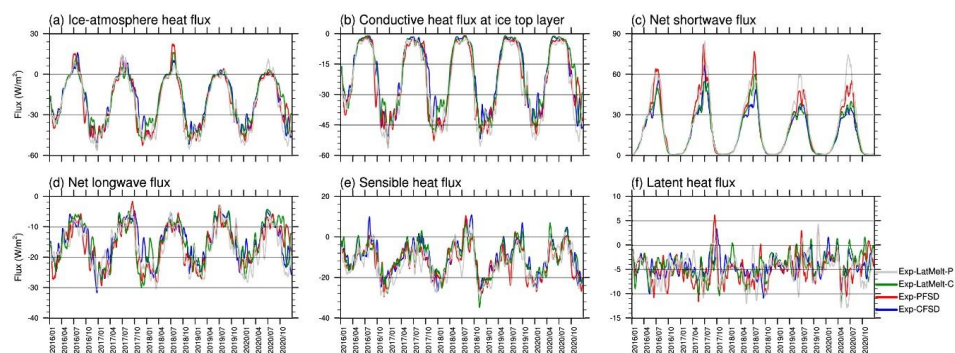
1069

1070 Figure 3 Time-series (15-day running-averaged) of sea ice mass budget terms for (a) Exp-
 1071 CFSD, (b) Exp-PFSD, (c) Exp-LatMelt-C, (d) Exp-LatMelt-P, (e) Exp-WaveFrac-P, (f) Exp-
 1072 WaveAtt-C, and (g) Exp-WaveAtt-P. Ice mass budget terms include: total mass change (black
 1073 line), sea ice melt at the air-ice interface (top melt, green line), sea ice melt at the bottom of the
 1074 ice (basal melt, red line), sea ice melt at the sides of the ice (lateral melt, grey line), sea ice
 1075 growth at the bottom of the ice (basal growth, blue line), sea ice growth by supercooled open
 1076 water (frazil, orange line), sea ice growth due to transformation of snow to sea ice (snowice,
 1077 light-blue line), and sea ice mass change due to dynamics-related processes (dynamics, purple
 1078 line) (Notz et al., 2016; Yang et al., 2022). For reference, snow melt term (yellow line) is
 1079 included.



1080

1081 Figure 4 Time-series (15-day running-averaged) of (a) ice-ocean heat flux, (b) friction velocity
1082 at ice-ocean interface, and (c) the temperature difference between SST and freezing point for
1083 Exp-CFSD (blue line), Exp-PFSD (red line), Exp-LatMelt-C (green line), and Exp-LatMelt-P
1084 (grey line). Note: (a) is positive downward and weighted by ice concentration.

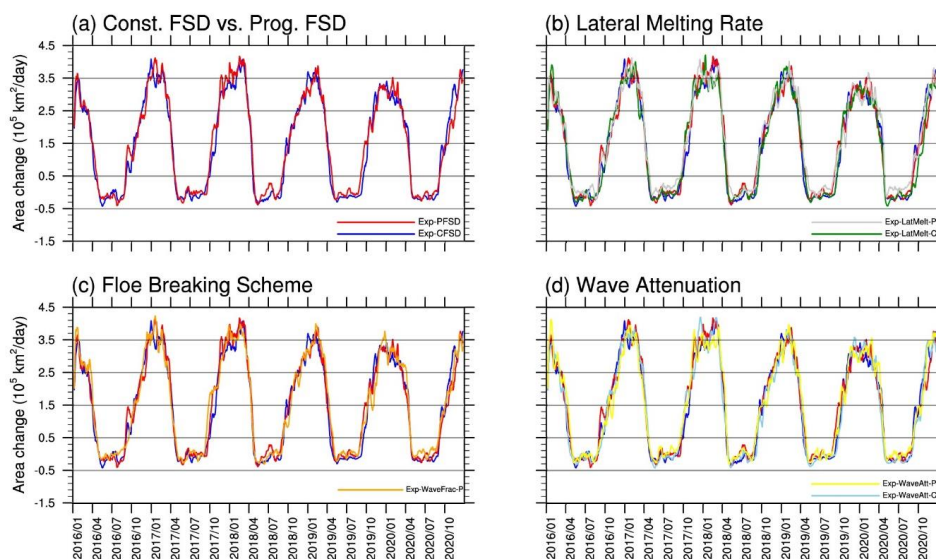


1085
1086
1087
1088
1089
1090
1091

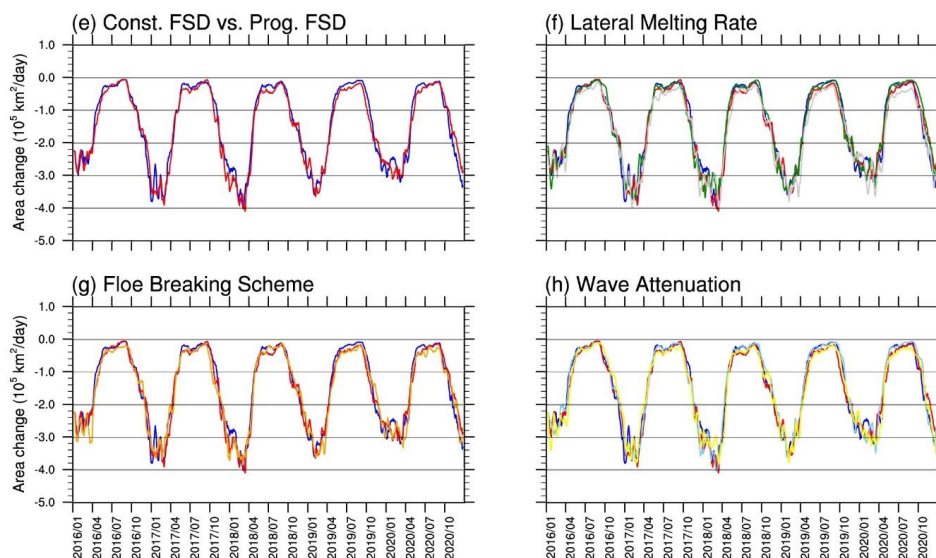
Figure 5 Time-series (15-day running-averaged) of (a) ice-atmosphere heat flux, (b) conductive heat flux at the ice top layer, (c) net shortwave flux, (d) net longwave flux, (e) sensible heat flux, and (f) latent heat flux for Exp-CFSD (blue line), Exp-PFSD (red line), Exp-LatMelt-C (green line), and Exp-LatMelt-P (grey line). Note: (a)-(e) are positive downwards and weighted by ice concentration.



Thermal Area Changes

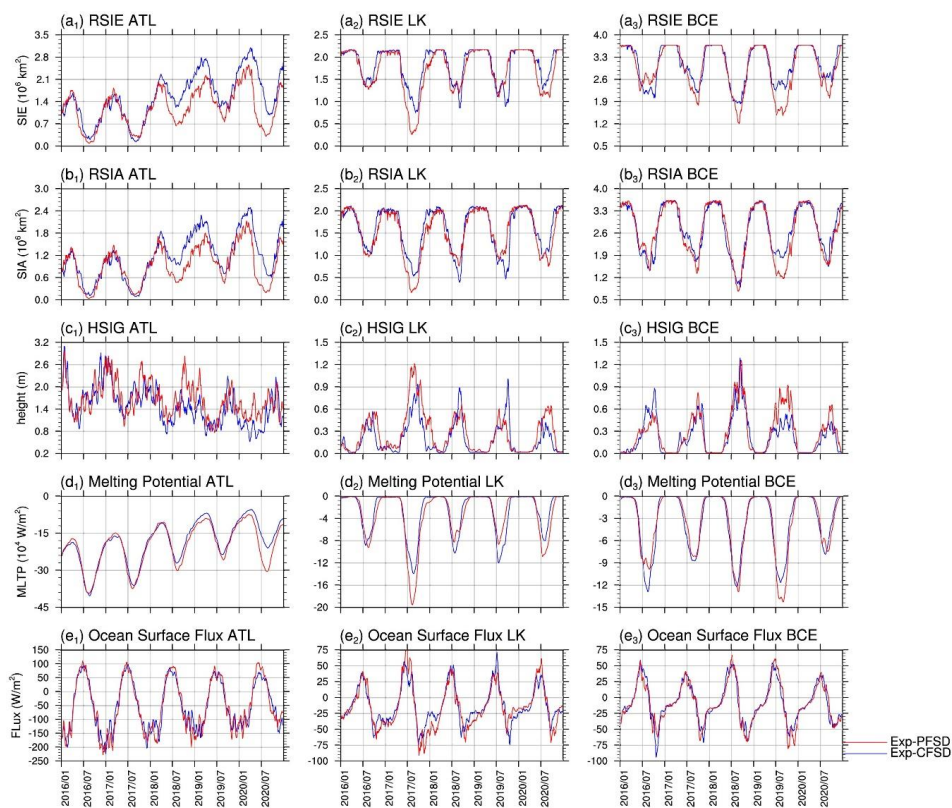


Dynamical Area Changes



1092

1093 Figure 6 Time-series (15-day running-averaged) of sea ice area changes due to thermal
1094 processes (a-d, upper panel) and dynamical processes (e-h, bottom panel) for Exp-CFSD (blue
1095 line), Exp-PFSD (red line), Exp-LatMelt-C (green line), Exp-LatMelt-P (grey line), Exp-
1096 WaveFrac-P (orange line), Exp-WaveAtt-C (light-blue line) and Exp-WaveAtt-P (yellow line).

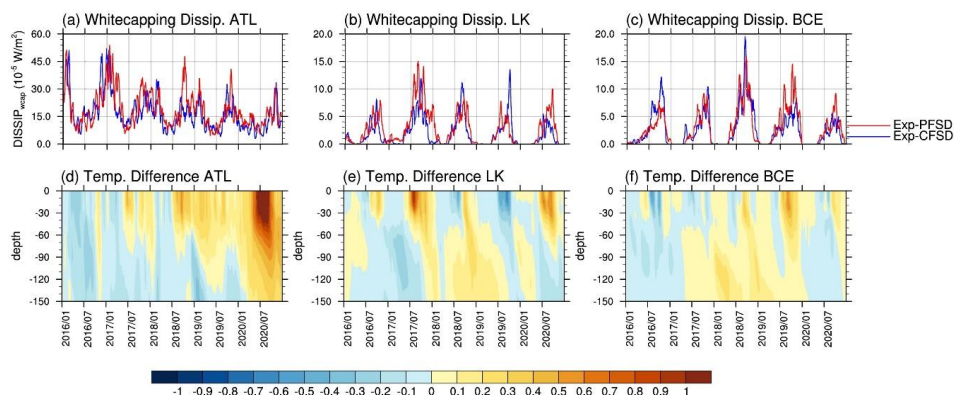


1097
 1098
 1099
 1100
 1101
 1102

Figure 7 Time-series of (a) ice extent, (b) ice area, (c) significant wave height, (d) melting potential, and (e) heat flux at the ocean surface in (1) ATL, (2) LK, and (3) BCE regions for Exp-CFSD (blue line) and Exp-PFSD (red line). Note: (c)-(e) are region-averaged and 15-day running-averaged values.

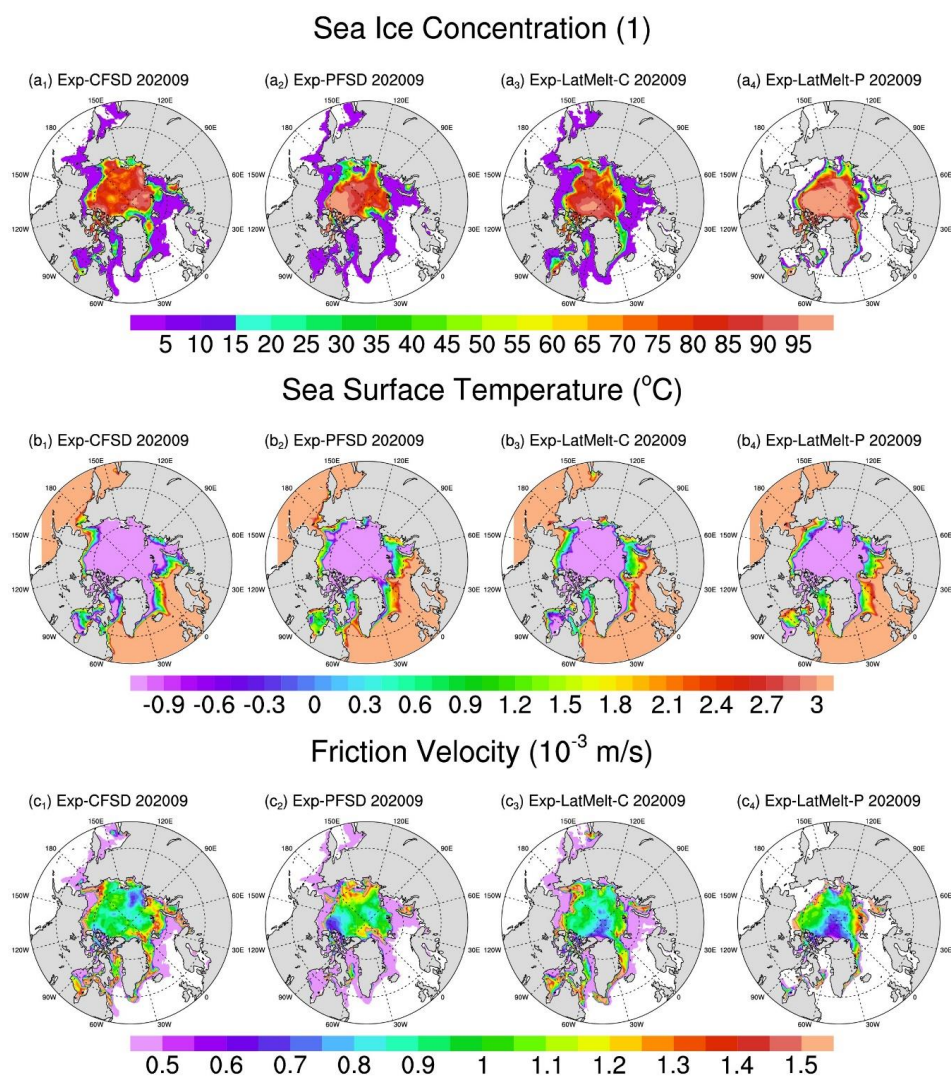


1103



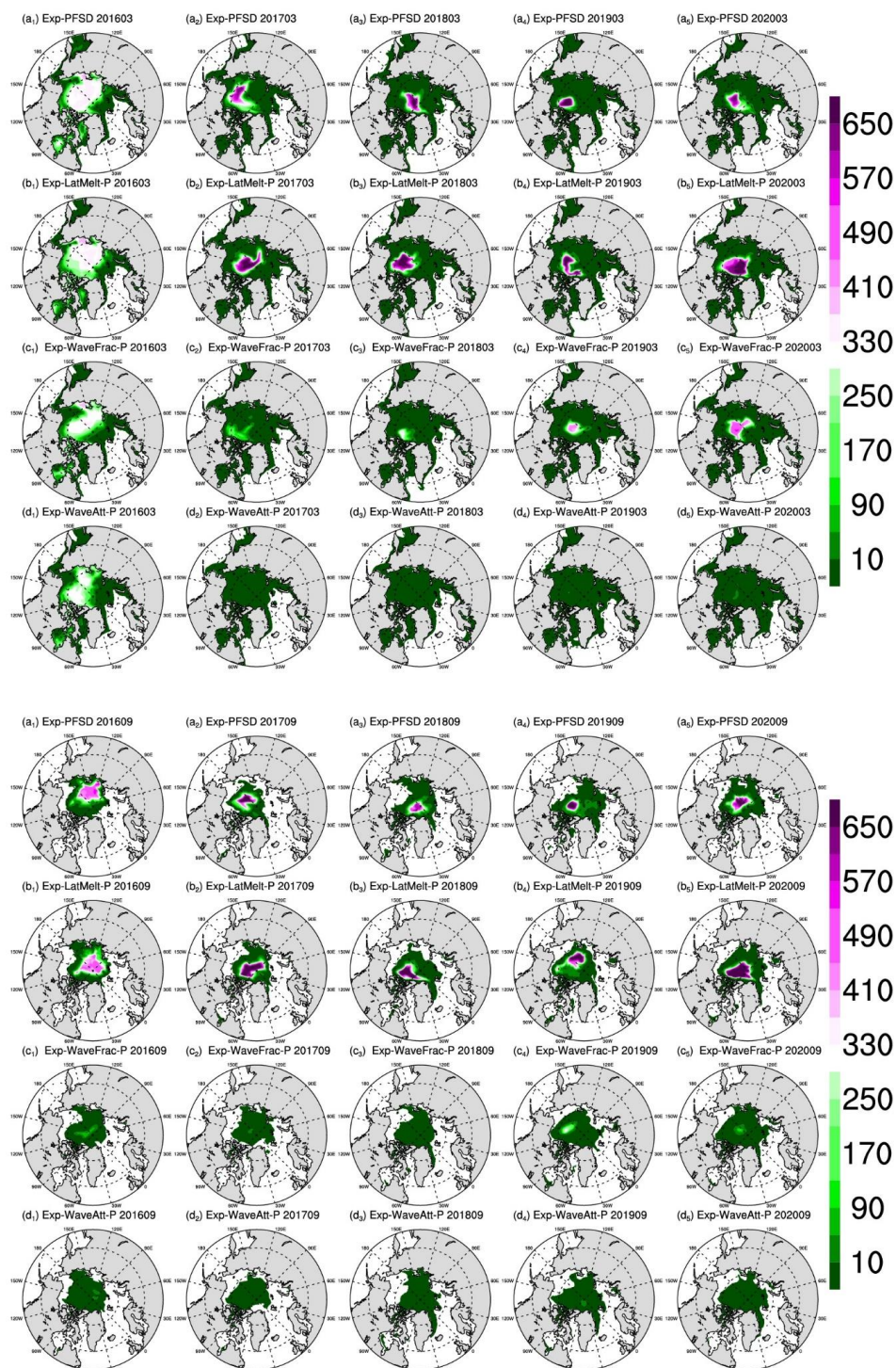
1104

1105 Figure 8 Time-series (15-day running-averaged) of white capping dissipation averaged over (a)
1106 ATL, (b) LK, and (c) BCE regions for Exp-CFSD (blue line) and Exp-PFSD (red line), and the
1107 temperature profile difference between Exp-CFSD and Exp-PFSD in the upper 150 m averaged
1108 over (d) ATL, (e) LK, and (f) BCE regions.
1109



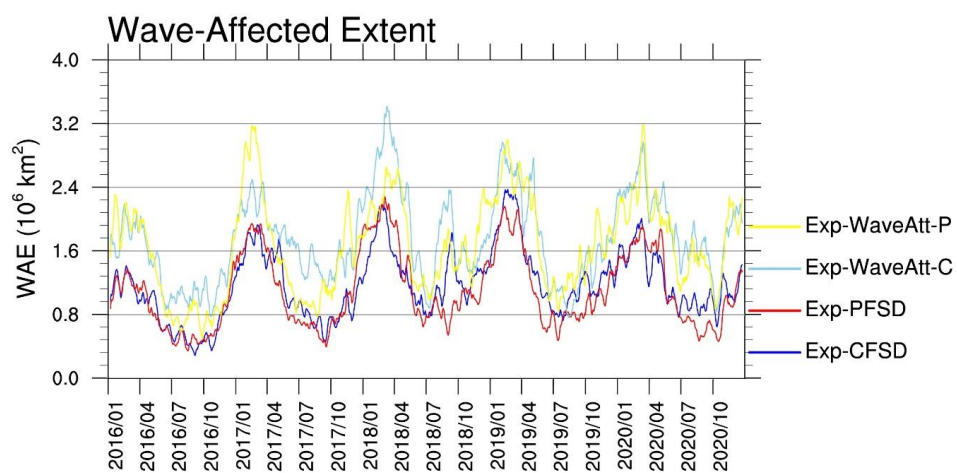
1110

1111 Figure 9 The monthly-mean of (a) sea ice concentration, (b) sea surface temperature, and (c)
 1112 friction velocity in September, 2020 for (1) Exp-CFSD, (2) Exp-PFSD, (3) Exp-LatMelt-C,
 1113 and (4) Exp-LatMelt-P.
 1114





1116 Figure 10 The spatial distribution of the representative floe radius in March (upper panel) and
1117 September (bottom panel) of (a) Exp-PFSD, (b) Exp-LatMelt-P, (c) Exp-WaveFrac-P, and (d)
1118 Exp-WaveAtt-P for 2016-2020. Note: cells with less than 15% ice concentration are treated as
1119 missing values.
1120



1121

1122 Figure 11 Time-series (15-day running-averaged) of Arctic wave-affected extent for Exp-CFSD
1123 (blue line), Exp-PFSD (red line), Exp-WaveAtt-C (light-blue line) and Exp-WaveAtt-P (yellow
1124 line).